

Evolving Synoptic Maps of the Solar Magnetic Field

John McCloughan

Supervisor: Assoc. Prof. Christopher Durrant

(2002)

A Thesis Submitted in Fulfilment
of the Requirements for the Degree of
Master of Science

University of Sydney
School of Mathematics and Statistics



Acknowledgements

There are many people I would like to thank for their help and support over the years, unfortunately I cannot recall them all here, to those people I may not mention here, but deserve it, thank you very much for all you have done.

Firstly, thank you to Associate Professor Chris Durrant for all your time and patience in helping me with my MSc project and thesis, which was both interesting and challenging. I am very grateful for having had such a wonderful supervisor to guide me through my Masters studies.

To my family; Pa, Dad, Mum, sister Judy, and to our late family friend Terry Mattick, thank you for all your love and for always supporting me through everything I ever choose to do.

To Mrs Helen McRae, thank you for inspiring me to continue in mathematics, your inspiration has set me on the journey of a life-time that I am now travelling, and would have otherwise not seen without your help and inspiration.

To the Department of Mathematics at the University Newcastle, thank you for everything you did for me throughout my undergraduate and honours degrees, and a special thank you to Dr Warren Wood who sparked my interest in Solar MHDs and kindly proof read this thesis.

To the School of Mathematics and Statistics at the University of Sydney, both academic and secretarial, thank you for all of your help and for making me feel welcome.

To my good friends, Leah Ratliff, Kathleen Humble, Tim Barry, Lydia Gaidell, Daniel McLean, Mathew Roth and Jo Sanders, thank you to each of you for being such wonderful friends and for always being there for me, I am eternally indebted to you and will always be there for each of you.

Thank you to the friends in the school that I have made in the two years that I have been at University of Sydney, including (from an exhaustive list) Fai Tsang, Shona Yu, Jon Dixon, Jonathan Tse, Hai Ho, Peter Moore, Tim Schaerf, William Bertram and James East, thank you for everything you have done for me, and for making my stay and studies here comfortable and enjoyable.

Thank you to all these people for everything, I am truly grateful to each and every one of you for the important and defining points that you have played throughout my life

Contents

Acknowledgements	1
Chapter 1. Introduction	3
1.1. Magnetograms	3
1.2. Synoptic Maps	4
Chapter 2. Background	8
2.1. Babcock's Model	8
2.2. Leighton's Random-Walk Model	10
2.3. NRL Flux Transport Models	13
2.4. Other Groups and The Flux-Transport Equation	24
Chapter 3. A Cartesian Model	32
3.1. The Instantaneous Map	33
3.2. The Time-Stepped Synoptic Map	34
3.3. The Analytic Version of the Synoptic Map	35
Chapter 4. The Synoptic Transport Equation	38
4.1. The flux-transport equation	38
4.2. Synoptic Maps	45
4.3. Evolution of Synoptic Maps	45
4.4. The Synoptic Transport Equation	46
Chapter 5. Implementation of the Synoptic Transport Equation	51

CONTENTS	2
5.1. Numerical Implementation of the Synoptic Transport Equation	51
5.2. A Synthetic Solar Model	55
5.3. Tests on the Synthetic Solar Model	57
5.4. Reconstructed Instantaneous Maps	65
Chapter 6. STE With Real Data	72
6.1. Simulating NSOKP Synoptic Maps	72
6.2. Reconstruction of Instantaneous Maps	79
Chapter 7. Conclusion	83
7.1. Concluding Remarks	91
Bibliography	93

CHAPTER 1

Introduction

This thesis investigates how magnetographic data may be used to study the long-term behaviour of the magnetic field distribution across the surface of the Sun. The solar magnetograph was designed primarily for measuring and mapping solar fields of from 1 to 20 gauss [Babc53]. Daily magnetograph observations of the full disc of the Sun were started from 1957. It is from these daily magnetograms that synoptic maps are constructed for the study of large-scale solar magnetic fields.

1.1. Magnetograms

Originally developed by Babcock [Babc53], the magnetograph is a powerful spectrograph, equipped with an analyser which alternates between the two senses of circular polarisation, which receives light from a selected part of the Sun's image. At the focus of the spectrograph, an exit slit is placed on a wing of a Fraunhofer line chosen for sensitivity to the Zeeman effect. Radiation transmitted by the second slit enters a device which measures the intensity of the light. If the longitudinal Zeeman effect now occurs, owing to a magnetic field in the Sun's atmosphere, a change of the analyser from the right-handed to the left-handed condition will produce a slight shift in the position of the line and will result in a corresponding change in the indication of the output. For a magnetic field of 1 gauss the line shift to be expected in the green region is 8×10^{-6} nm. When the Zeeman effect is observed in these measurements, the displacements measured are proportional to $H \cos \gamma$, the component of the field in the line-of-sight, where γ is the angle of the vector field direction from the line-of-sight.

1.2. Synoptic Maps

Synoptic maps of the solar magnetic fields are currently produced by

- National Solar Observatory at Kitt Peak (NSOKP),
- Mount Wilson Observatory (MWO),
- Wilcox Solar Observatory (WSO),
- Global Oscillation Network Group (GONG), and
- SOHO’s Michelson Doppler Imager.

For the period of this study synoptic maps and magnetograms from NSOKP were utilised [**Web1**]. The techniques used by NSOKP and MWO to produce synoptic maps from magnetograms differ in a number of respects. The daily magnetograms at NSOKP are produced by a spectromagnetograph which is arranged to produce a spectrum centred on one of 854.2 nm CaII, 868.8 nm FeI, or 1083 nm HeI [**Web1**]. As described by Worden and Harvey [**Word00**], the NSOKP synoptic maps are constructed from these daily longitudinal magnetograms by firstly “secantising” the magnetogram fields, that is, assuming that the fields are radial to the solar surface and multiplying the observed fields by $\sec(\mu)$ where μ is the angle between the line of sight and the normal to the surface at the point of observation. The synoptic maps are constructed by making a weighted average of the secantised fields at each Carrington longitude using an algorithm which optimises the contribution of the surface fields at the central meridian, these are re-mapped into heliocentric sine-latitude and longitude, and are “added” together by cutting and pasting the Carrington longitude near the central meridian of each image with those of the full Carrington synoptic map. For example, Figure 1.1 shows three magnetograms of a sequence for CR 1918, the corresponding synoptic map in the centre and the sine-latitude and longitude plot at the bottom each produced by NSOKP.

FIGURE 1.1. Three selected magnetograms of CR 1918 (top) are placed in relative correspondence to the longitudes of the sine-latitude and longitude synoptic map (centre) which they constitute. The bottom plot is the corresponding latitude and longitude plot utilised for simulation purposes. Each were produced by NSOKP.

The magnetograph at MWO observes the magnetic field simultaneously for several lines, one of which is 525.02 nm FeI, to measure the longitudinal component of the Zeeman effect [Web2]. The synoptic maps are built up using all observations available for each point of the solar surface during a specified Carrington rotation. The point position is based on its Carrington co-ordinates at the time of central meridian passage. Observations taken when the point is not on the central meridian are corrected for differential rotation to obtain the position which corresponds to that at the central meridian passage. The measurement is the weighted average of all these observations using a weighting function which is the cosine of the central meridian distance. Corrections are made to compensate for the change in the spectral line profile and for scattered light.

Synoptic maps indicate measurements of the distribution of the line-of-sight component of magnetic flux on the solar surface observed near the central meridian. Whereas, the full map over the whole surface at any instant is termed an *Instantaneous map*. Thus a synoptic map for a particular Carrington rotation does not represent a “photograph” of the solar surface at any instant in time during that rotation, but instead provides a record of the averaged fields as they cross the solar disc during that rotation with emphasis upon their central meridian passage.

The large-scale patterns in the photospheric magnetic field are important for the studies of stellar magnetic activity and dynamo [Schr00]. Many detailed studies utilising synoptic maps have been carried out, such as

- boundary conditions for modelling the solar coronal magnetic fields,
- modelling the structure and dynamics of solar winds,
- evolution and transport of magnetic flux during the solar cycle.

This thesis investigates simulations of the evolution of synoptic maps utilising the flux-transport equation, and presents the derivation of the correct synoptic evolution equation, the synoptic transport equation.

Chapter 2 is a background Chapter outlining the last two decades of research which developed the flux-transport equation model and the applications it has enjoyed.

Chapter 3 describes a simple Cartesian model which illustrates the inherent error in applying the flux-transport equation to synoptic maps.

Chapter 4 presents the derivation of the synoptic transport equation in spherical co-ordinates.

Chapter 5 describes the implementation of the synoptic transport equation scheme and its application to synthetic synoptic maps which results in extremely accurate predictions of the true synthetic synoptic and instantaneous maps.

Chapter 6 exhibits the application of the synoptic transport equation to real data from NSOKP.

Chapter 7 summarises the underlying conclusions from this project and indicates future research prospects.

CHAPTER 2

Background

Two major contributions in the early investigations of the solar activity cycle were Babcock's (1961) empirical model of the topology of the solar surface magnetic fields in which he suggested the existence of meridional flow, and Leighton's (1964) heuristic model, which disregarded the *ad hoc* hypothesis of bulk meridional flow, implemented a diffusion equation with the combined effects of supergranulation diffusion and differential rotation. DeVore *et.al.* (1984) of the Naval Research Laboratory (NRL) group mathematically demonstrated a derivation of the flux-transport equation from the magnetic induction equation that incorporated a meridional circulation flow. Since then the flux transport equation and meridional circulation have both been applied to examining different aspects of solar surface activity. This chapter summarises the work done by Babcock, Leighton and the NRL group which lead to the development of the flux-transport equation, and then presents a brief overview of the diverse applications of the flux-transport equation in the study of the evolution of the solar magnetic fields.

2.1. Babcock's Model

In 1961 Babcock developed an empirical model of a dynamo process to account for the cyclically varying configuration of the Sun's magnetic field [**Babc61**]. He attempted to account for a number of crucial observations of features during the solar cycle such as the reversal of the main dipolar field, Spörer's Law of sunspot

latitudes (spot groups tend to emerge at progressively lower latitudes as a cycle progresses [Schr00]), Hale's Law governing the magnetic polarity of sunspots, chromospheric whirls, recurrence of sunspots in preferred zones, and the fact that bipolar magnetic regions (BMRs) disappear by expanding.

The initial field of the Babcock model approximates an axisymmetric dipole with lines of force lying in meridional planes. The poloidal field is wound by the differential rotation into a spiral formation with a strong toroidal component. As the winding increases, kinks (or ropes) form and the magnetic buoyancy lifts them to the surface as active regions. Considerable randomness in time and location of BMRs follows from the disturbances due to the twisting and convection of the flux ropes and to the gradual reduction of the amplification process whenever BMRs are formed. The BMRs, according to this model, account for a number of observed phenomena in the variations in the solar cycle, as listed before. Then the neutralisation and reversal of the main dipolar field is related to the dispersal of magnetic flux of disappearing BMRs, the lifetime of each of which measured in weeks or months, and finally to the cumulative effect of thousands of BMRs that occur in the course of a sunspot cycle. During neutralisation, the fields are generally weak and there is frequent interference from adjacent regions. According to Hale's law, spots tend to occur in bipolar groups with "preceding" (p) and "following" (f) members (in the sense of East-West rotation) showing opposite polarity. An essential feature of the model is the tilt of the BMRs, the following polarity emerges closer to the pole than the preceding, therefore the following polarity reaches the pole first. As more and more BMRs form, grow, and vanish, the initial dipolar field of the model is first neutralised by poleward drift of the f -parts of BMRs and supplanted by a new dipolar field of opposite polarity. Neutralisation is effected at the time of sunspot maximum and the new, reversed field is in evidence shortly after. The reversed dipolar field is the residual of the foregoing

process. It is attained in full after about 11-years and is similar to the initial stage except for the reversed polarity. The differential rotation continues in the same sense, so that the analogues to this whole process take place again to complete the whole 22-year magnetic cycle, with return of configuration of the field to that of the initial field.

Babcock made the suggestion that “The cause of the migration in the latitude of the respective parts of BMRs remains rather obscure but this migration implies the existence of meridional flow toward the equator at lower latitudes and towards the poles in the moderate latitude”.

2.2. Leighton's Random-Walk Model

Leighton agreed that Babcock's model accounted quite satisfactorily for Spörer's Law and Maunder's “butterfly” diagram, Hale's law of polarity, and the relevant number of sunspots at each stage in a cycle. Leighton wrote his 1964 paper [Leig64] to further clarify one important aspect of the solar cycle - the expansions and apparent “migration” of unipolar and bipolar magnetic regions. The principal basis of the study was the discovery of a second convective circulatory field in the Sun called the supergranulation. The supergranulation velocity field was shown to be responsible for the reticular structure of the chromospheric network. A key feature is that the cellular circulatory motions concentrate the weak, large-scale field of a magnetic region into the narrow lanes at the boundaries of the convective cells. Because of its non-stationary nature, the velocity field will move a given element of gas about on the Sun in a random walk. Due to the relatively great electrical conductivity of the solar matter, a magnetic field which projects through the surface will tend to be dragged laterally by the ionised material and will therefore become displaced as well. To this extent magnetic lines of force were regarded as corresponding to a special kind

of “atom” in the solar atmosphere, so far as its lateral movement is concerned. The nearly-equal dispersal rates of ordinary granulation and supergranulation appeared to indicate that both velocity fields should be effective in the development of BMRs. However, Leighton suggested that only the large-scale, more deeply rooted, supergranulation motions are sufficiently coupled with the magnetic lines of force to move the BMRs about the Sun. Leighton had suggested this since, at the time, there was no evidence that the ordinary granulation concentrated magnetic field significantly at its boundaries, whereas the chromospheric network, which outlines the distribution of magnetic flux, was known to correspond to the supergranulation cell boundaries. Observations showed well-defined and stable boundaries between the two opposite-polarity regions, often marked by disc filaments. Thus Leighton assumed that a composite region was describable as a linear superposition of separate parts of opposite polarity, each of which develop independently of each other; the resulting field of two expanding overlapping regions is the algebraic sum of the two separate fields.

2.2.1. The Random Walk as a “Diffusion” Process. The random walk process is a two-dimensional analogue of the process by which molecules of a gas migrate and intermix. In the context of this analogy, Leighton maintained much of the terminology and concepts relating to the molecular case. Two concepts were explicitly mentioned; the average lateral drift rate of the lines of force C were suggested to be analogous of a “current” which spreads out as a result of a “concentration gradient” of “atoms” of a particular kind, and the “mixing coefficient” D , which is related to scale and lifetime of the supergranulation field, was described as an analogy of the diffusion coefficient of a molecular gas. The number surface density n of points at which lines of force enter the Sun can be regarded as corresponding to the concentration of objects whose diffusion is of interest, the lines of force. Also the average lateral drift rate C of the lines force are considered to be proportional to the gradient of the concentration

$C = -D\nabla n$. But the conservation of magnetic flux implies an equation of continuity

$$\frac{\partial n}{\partial t} + \nabla \cdot C = 0$$

Thus

$$\frac{\partial n}{\partial t} = D\nabla^2 n$$

is the diffusion equation for n . The mixing coefficient D may be expressed in terms of step length L and rate N , of lateral steps per unit time, in analogy with the relation between mean free path λ and collision rate τ^{-1} . According to Leighton the relation in two dimensions is $D = \frac{1}{2}L^2N$. In spherical co-ordinates for a sphere of radius a

$$\frac{\partial n}{\partial t} = \frac{D}{a^2} \left[\frac{1}{\sin \theta} \frac{\partial}{\partial \theta} \left(\sin \theta \frac{\partial n}{\partial \theta} \right) + \frac{1}{\sin^2 \theta} \frac{\partial^2 n}{\partial \phi^2} \right].$$

In the solar case the diffusion, or random walk, process is modified by the bodily drift due to differential rotation. If \mathbf{v} is drift velocity then the modified diffusion equation is

$$\frac{\partial n}{\partial t} = D\nabla^2 n - (\mathbf{v} \cdot \nabla)n.$$

In spherical-polar co-ordinates, with $\mathbf{v} = \omega(\theta)a \sin \theta \mathbf{e}_\phi$ where $\omega(\theta)$ is angular velocity of differential motion at co-latitude θ

$$\frac{\partial n}{\partial t} = \frac{D}{a^2} \left[\frac{1}{\sin \theta} \frac{\partial}{\partial \theta} \left(\sin \theta \frac{\partial n}{\partial \theta} \right) + \frac{1}{\sin^2 \theta} \frac{\partial^2 n}{\partial \phi^2} \right] - \omega(\theta) \frac{\partial n}{\partial \phi}.$$

The major effect of drift is to deform the expanding region, elongating it in longitude and “tilting” it because of the θ -dependence of ω . The north-south progress of diffusion is not affected by differential rotation.

2.2.2. The Average Effects of Many Bipolar Spot Groups. Spot groups tend to appear mostly within certain restricted regions of latitude in each hemisphere. The “preceding” p and “follower” f parts of a spot group are generally separated a few degree in longitude, and follow Hale’s law of polarity. It had also been observed

that the p and f parts of a spot group tended to be separated in latitude. Because of the reversed polarity in opposite hemispheres the magnetic dipole moments of the spot groups in both hemisphere tend to have meridional components of the same sign. The random-walk process should thus lead to a large-scale dipole-like field whose sign is that of this meridional component, and this was in agreement with observation. In the random walk model, characterised by a single parameter D which Leighton determined to be in the range of $770 - 1540 \text{ km}^2\text{s}^{-1}$, magnetic lines of force which enter or leave the solar surface are independently moved about in a two dimensional random walk and are also transported systematically in longitude by solar differential rotation. In view of the excellent agreement of the simple random-walk model with observations, Leighton concluded that meridional currents proposed by Babcock were unnecessary in order to transport magnetic flux on the Solar surface.

2.3. NRL Flux Transport Models

Leighton had proposed that the net effect of the non-stationary supergranulation convective motions caused the large-scale field to spread out over the solar surface with time in analogy to scalar diffusion. In 1984 the Naval Research Laboratory (NRL) group mathematically derived the diffusion equation presented in Leighton's paper, from the magnetic induction equation. The resulting equation they called the flux transport equation which was equivalent to Leighton's transport equation

$$\frac{\partial B}{\partial t} + \nabla \cdot (B\mathbf{v}_s) = \kappa \nabla_s^2 B$$

where B is the magnetic flux density through the surface, \mathbf{v}_s is the large-scale surface velocity field, κ is the diffusion constant characterising the mixing and spreading of the large-scale magnetic field by the supergranulation, and ∇_s is the Laplacian operator on the surface of the sphere. In the meantime, independent studies (see references in [DeVo85]) had suggested the Sun had a poleward meridional flow of magnitude

$10 - 20 \text{ ms}^{-1}$, and Giovanelli [Giov85] proposed the incorporation of meridional flow into the solar cycle. Thus the NRL group developed the flux-transport equation in which \mathbf{v}_s had differential rotation and meridional flow components, unlike Leighton's model where he only used a differential rotation term. The NRL group have produced an enormous amount of work studying the solar magnetic fields on the basis of the flux-transport equation. This section splits their work into two sets based upon the technique that was used, the first set of papers was based upon magnetograms, whilst the second set of papers was based upon synoptic maps.

2.3.1. Evolution Studies based on Magnetograms. In their 1984 paper [DeVo84] the NRL group stated that the differential rotation has no effect on an axisymmetric magnetic field $B(\theta, t)$ and wrote Leighton's induction equation in spherical co-ordinates,

$$\frac{\partial B}{\partial t} + \frac{1}{R_\odot \sin \theta} \frac{\partial}{\partial \theta} (Bv(\theta) \sin \theta) = \frac{\kappa}{R_\odot^2} \frac{1}{\sin \theta} \frac{\partial}{\partial \theta} \left(\sin \theta \frac{\partial B}{\partial \theta} \right)$$

where θ is the co-latitude angle and $v(\theta)$ is large scale meridional circulation speed. They firstly determined analytic solutions to the transport equation for different meridional flow profiles. In particular, in the absence of meridional flow, $v_o = 0$, Leighton's solutions for diffusivity transport on a sphere were recovered. The transport equation was then solved as an initial valued problem by initialising the field as a dipole distribution and integrating forward in time, assuming that the rate of emergence of new large-scale sources of flux on the Sun near sunspot minimum is sufficiently low to be neglected. They continued simulations until all transients had decayed away and the field profile had settled to its asymptotic state. The NRL calculations showed that a meridional flow had a significant effect on the large-scale magnetic field distribution during an extended interval of very low or zero sunspot number, such as near sunspot minimum.

Using full-disc magnetograms DeVore *et al.* [**DeVo85**] simulated the evolution of several observed solar active regions by solving a transport equation, and obtained parameters for the flux transport which were in quantitative agreement with earlier investigators as quoted in their paper. The transport equation including meridional flow and source term was first presented in the NRL's 1985 paper [**Shee85**], which for a Sun-centred spherical co-ordinate system is

$$\begin{aligned} \frac{\partial B}{\partial t} = & -\omega(\theta) \frac{\partial B}{\partial \phi} - \frac{1}{R_{\odot} \sin \theta} \frac{\partial}{\partial \theta} (Bv(\theta) \sin \theta) \\ & + \frac{\kappa}{R_{\odot}} \left(\frac{1}{\sin \theta} \frac{\partial}{\partial \theta} \left(\sin \theta \frac{\partial B}{\partial \theta} \right) + \frac{1}{\sin^2 \theta} \frac{\partial^2 B}{\partial \phi^2} \right) + S(\theta, \phi, t) \end{aligned}$$

where B is the magnetic flux density through the solar surface, κ is the diffusion characterising the mixing and spreading of the large-scale magnetic field by the supergranulation, $S(\theta, \phi, t)$ is a source function representing emergence of new bipolar magnetic regions, ϕ is the azimuthal angle measured westward from the sub-Earth longitude (central meridian), and $\omega(\theta)$ is the latitude dependent synodic rotation rate. This is what the NRL group termed as the *flux-transport equation*.

The NRL group continued their investigations of the simulations of the solar magnetic fields during sunspot cycle 21 and published a paper in 1987 which followed a similar procedure. They specified an initial distribution of flux, profiles of rotation and meridional flow, and a value for the rate of diffusion and a record of the sources of new flux [**DeVo87**]. At each time incremented step, the field was then transported over the surface in response to rotation flow, diffusion, and newly emerged sources were added. The solar rotation was taken according to Snodgrass' rate [**Snod83**]

$$\omega(\theta) = 13.38 - 2.30 \cos^2 \theta - 1.62 \cos^4 \theta \text{ deg day}^{-1}$$

and a simple hypothetical profile for the meridional flow was adopted

$$v(\theta) = v_o \left(\frac{(p+1)^{(p+1)/2}}{p^{p/2}} \sin^p \theta \cos \theta \right)^q$$

in the northern hemisphere. The flow was assumed to be antisymmetric across the equator, and to vanish at the poles and the equator. The shape of the profile is governed by the parameter p , which determines the co-latitude θ_o at which the flow speed reaches its peak value $\arctan(p^{1/2})$, and by the parameter q , which determines the full width at half maximum. In June and December the Earth passes through the Sun's equatorial plane, so averaged fields measured at the central meridian at polar latitudes during these months are used to calibrate the results. After experimentation with parameters of the velocity profile it was found that a suitable characterisation was given by $v_o = 10$, $p = 99$ and $q = 0.04$. The flow reaches a peak speed of 10 ms^{-1} at 5.7° latitude and falls off rapidly to zero at polar latitudes. Two empirical rules were found

- (1) Profiles of fixed breadth; as the latitude of the peak flow is shifted poleward, the peak speed must be decreased to accomplish the polarity reversal at the appropriate time.
- (2) Profiles with fixed latitudes of peak flow; as the profile is broadened, the peak flow speed must be reduced to accomplish the polarity reversal at the appropriate time.

From this study it was concluded that transport of flux by a poleward meridional flow reinforces the diffusion of flux toward polar latitudes. These effects substantially alter the long term evolution of a BMR and its ultimate contribution to the polar fields. Though the following flux reaches the polar latitudes quicker and at greater strength, there is more preceding flux to cancel the following flux. The resulting net flux is weaker and the polar fields are reduced in strength.

A number of investigators during the period 1979-1988 reported observational evidence for a poleward bulk flow of 10 ms^{-1} or more. At the same time, evidence had been mounting that the polar fields are highly concentrated near sunspot minimum which points to the presence of a large-scale poleward flow. The strongly peaked nature of the polar fields near sunspot minimum conflicted with Leighton's model. Thus the NRL group continued to develop the flux transport model in an attempt to account for the structure and evolution of polar fields including the effect of meridional flow. Wang and Sheeley [**Wan89a**] found the following complementary processes act to build up the polar field.

- (1) The eruption of BMRs with their leading polarity flux systematically equatorward of their trailing polarity flux establishes an overall separation of polarities in latitude. Supergranulation diffusion contributes to this separation by wiping out the minority polarity in each majority polarity zone,
- (2) Supergranulation diffusion preferentially annihilates the lower latitude, leading polarity fluxes in the two hemisphere by merging them across the equator,
- (3) Meridional flow is the primary means of transporting the resulting surplus of trailing polarity flux in each hemisphere to the poles, and concentrates it there against the spreading effect of supergranulation diffusion.

It was concluded that diffusion plays an essential role in creating the polar fields by efficiently annihilating leading flux around the equator, especially after sunspot maximum when flux erupts at lower latitude. This leaves a net surplus of trailing flux in each hemisphere, which is carried to the poles by meridional flow with only minor assistance by diffusion. If supergranulation diffusion did not exist, meridional flow would convect equal amounts of leading and trailing flux to the poles, producing no net change in the polar fields. If meridional flow were absent, a high diffusion rate would itself reverse the polar fields, in accordance to Leighton's supergranulation

model. Even greater surplus of trailing flux would be produced because leading flux would freely cross the equator and be annihilated. The trailing flux would spread poleward and establish a strong dipole moment toward sunspot minimum. However, discrete poleward surges would not occur and the final field distribution would not be strongly concentrated toward the poles as observed.

Next Sheeley *et al.* [Shee89] examined the magnetic field line connections that are produced between evolving BMRs and the nearby polar magnetic field. The reference calculations were made in which the polar field had a concentrated form and idealised magnetic doublets were introduced as estimates for new large BMRs. Using the flux-transport equation, the resulting configurations were evolved under the combined influences of supergranulation diffusion at the rate $\kappa = 600 \text{ km}^2\text{s}^{-1}$, poleward meridional flow at the speed $v(\theta) = -5 \text{ ms}^{-1} \sin(2\theta)$, and differential rotation at the Snodgrass rate.

Wang and Sheeley [Wang90] investigated how sunspot activity and magnetic flux transport determine the evolution of coronal holes and their wind streams. They used numerical simulations to examine the relationship between the transport of flux from active regions and the formation and evolution of coronal holes. Assuming an initial field configuration and using doublet sources to represent new emerging active regions, the flux-transport equation was numerically solved with $\kappa = 600 \text{ km}^2\text{s}^{-1}$. Meridional flow $v(\theta)$ was assumed to peak at 6° from the equator with a speed of 10 ms^{-1} . The NRL group concluded from this study that

- Supergranulation Diffusion spreads active region flux over the solar surface and wipes out pockets of mixed polarity, thus creating large unipolar areas containing open field lines. The reversal of the polar fields and the establishment of the new cycle polar holes are made possible by the diffusive

annihilation of leading-polarity flux at the equator, which leaves a surplus of trailing-polarity flux in each hemisphere.

- Differential Rotation spreads flux in longitude. The rotational shearing, which is strongest at mid-latitude, accelerates the decay of mixed-polarity regions and symmetrises the flux distribution. Differential rotation combines with diffusion to create axisymmetric polar holes from the original active-regions fields.
- Meridional flow (i) increases the decay of low-latitude holes by transporting flux to mid-latitudes, where the non-axisymmetric component of the field is annihilated by shearing and diffusion, (ii) concentrates the remaining flux at the poles, preventing polar holes from spreading to lower latitudes, and (iii) impedes the cancellation of leading-polarity flux across the equator, limiting the growth of trailing-polarity holes.

Next Wang and Sheeley [**Wan91a**] considered how to determine a mechanism for the generation of the Sun’s large-scale poloidal magnetic field in the general framework of the Babcock-Leighton model. They identified two distinct contributions to this process, the axial tilts of BMR as they erupt at the solar surface, and the subsequent transport of erupted flux over the surface. Transport processes redistribute magnetic flux over the solar surface, and thereby modify the contribution of the “intrinsic” BMR dipole strengths to the Sun’s total dipole moment. This effect was studied by numerically solving the flux-transport equation with $\kappa = 600 \text{ km}^2\text{s}^{-1}$, and peak flow speed of $v_0 = 10 \text{ ms}^{-1}$ at 6° latitude. The initial photospheric field in August 1976 was taken to be of the form $\pm 11.5 \cos^8 \theta$ gauss and ~ 2700 empirically determined sources from WSO magnetograms were deposited at their observed latitude and time of eruption. The calculations were run until 1987 with the deposit of sources stopped at April 1986 to illustrate “turning off” the source term. Different values

of v_0 were considered. The best overall agreement was obtained with $v_0 = 10 \text{ ms}^{-1}$. In addition to the “regular” 2700 BMRs, they also simulated ephemeral regions by depositing large numbers of randomly orientated bipoles. It was concluded that the eruption of large numbers of randomly orientated ephemeral regions does not produce an effect equivalent to supergranulation. In particular, ephemeral regions do not act to transport flux systematically across latitudes, nor do they cause the large-scale field to decay.

Wang *et.al.* [Wan91b] studied the dependence of the magnetic field evolution on the choice of parameters such as diffusion and flow speed, κ , p , q , v_o , and σ (rate at which flux erupts on the solar surface). Using a similar initial field to [Wan91a] the flux-transport equation was employed to simulate the solar cycle, assuming the source was

$$S(R_\odot, \theta, t) = \frac{\epsilon h R_h}{2\pi R_\odot^3 \sin \theta} \frac{\partial}{\partial \theta} \left(\frac{B_\phi a \sin \gamma}{\tau} \right)$$

where a is the linear pole separation of a BMR formed from the subsurface toroidal field, γ is its angle of tilt relative to the east-west line, τ is the time scale for the BMR to erupt, and ϵ is a numerical constant which is at most of order unity. For the toroidal field, B_ϕ , they included in the flux-transport equation both a subsurface flow and a turbulent diffusion term. It was found that the latitudinal gradient in the rotation rate generates toroidal flux from the subsurface meridional field; the toroidal flux erupts in the form of BMRs and acts to reverse the underlying meridional flow. The toroidal flux is convected and intensified from the mid-latitudes to the equator, thus maintaining globally periodic oscillations. A small amount of turbulent diffusion is required to limit the growth of the toroidal field by merging it with its counterpart in the opposite hemisphere.

2.3.2. Evolution Studies based on Synoptic Maps. The first appearance of an application of the flux-transport equation to study the evolution of the solar surface

magnetic fields based upon synoptic maps was the NRL 1985 paper [Shee85] which presented simulations of the solar magnetic field during the first eight years of sunspot cycle 21. The flux-transport equation was used to calculate the radial field on a full two-dimensional grid. Synoptic maps from NSOKP were chosen for an initial surface flux distribution. Specific profiles of differential rotation and meridional flow, and specific values for the diffusion constant were assumed. By using the flux-transport equation this “initial” synoptic map was advanced in small time increments (such as a day) in order to compute changes in the large-scale magnetic field. For realistic comparison with observed fields, approximately 2500 BMRs were entered into the simulations at times close to their appearance on magnetograms during the interval. After varying the transport parameters and source properties it was concluded that, at first differential rotation was the dominant means of decay for lower-order modes of the field but meridional flow surpasses differential rotation as a means for decay after a time on the order of $\frac{R_{\odot}}{2v_0}$, where v_0 is the peak meridional flow speed, by which time it will have carried most of the flux to high latitudes. Diffusion was found to be the least effective mechanism for decay of lower order modes of the field but the most effective mechanism for the decay of higher order modes of a new BMR. Furthermore, newly emerging magnetic regions are essential for replenishing the surface flux and maintaining the mean field against decay.

The first use of the approach of using synoptic maps to make detailed studies of structures on the solar surface was Sheeley *et.al.* [Shee87]. They studied the rotational influence of supergranular diffusion, meridional flow, and flux eruptions using simulations on sunspot cycle 21 synoptic maps. The NSOKP synoptic maps were used as if they were “instantaneous maps” and were compared with simulations produced with the flux-transport equation using assumed transport parameters and source properties. It was noted that there was a significant discrepancy in results at

latitudes greater than $\sim 30^\circ$, and that the simulated polar field reversed too early with a strength greatly exceeding that of the observed field.

Carrying out more numerical simulations Wang *et al.* [Wan89b] investigated the evolution of individual active regions and then how the supergranular convective motions and meridional circulation, interact over the 11-year sunspot cycle to affect the polar field. They conceded that it is only on scales exceeding the supergranular size that a description of the magnetic flux transport in terms of diffusion and meridional flow becomes meaningful. For the detailed study of the decay of active regions, a number of regions were selected from observations which consisted of synoptic maps of the line of sight photospheric field, compiled at MWO and WSO. The large-scale field was assumed to be primarily radial at the photosphere, as inferred observationally. The photospheric field strengths were divided by $\sin \theta$ to convert the line-of-sight values into radial ones and then interpolated onto 128×64 numerical grid. The map containing the first central-meridian passage of the active region under study was used as the initial field configuration in the simulation. This photospheric map was evolved according to the flux-transport equation, with $S(\theta, \phi, t) = 0$, and trial values of the parameters κ and v_0 adopted. For the study of the meridional flow and the polar field, an initial field configuration was taken to be of the form $\mathbf{B} = \pm 11.5 \cos^8 \theta$ gauss in agreement with WSO measurements, and was evolved according to the flux-transport equation from Aug 1976-Apr 1978 with magnetic doublet sources deposited onto the computational grid at the observed locations and time of eruption. The strengths of the 2800 doublet sources used in the simulations were estimated empirically from NSOKP daily magnetograms. Different κ , v_0 , p and q were used and each case was compared with WSO synoptic observations of the photospheric field during sunspot cycle 21. The best fits to both the average long-term evolution of the dipole field and

the final latitudinal distribution of the axisymmetric field are provided by a diffusion rate $\kappa = 600 \text{ km}^2 \text{ s}^{-1}$ combined with a poleward flow of amplitude 10 ms^{-1} . The combination of large diffusion and poleward flow rates represents a compromise that leads to both a strong dipole moment and sharply peaked polar field. Allowing for systematic errors in the determinations of the dipoles, they estimated the uncertainty in these quantities to be $\pm 200 \text{ km}^2 \text{ s}^{-1}$ and $\pm 3 \text{ ms}^{-1}$. High-latitude field strengths measured at MWO were less than two-thirds of WSO strengths for the same period, and would imply lower transport rates, $\kappa = 300 \text{ km}^2 \text{ s}^{-1}$ and $\pm 7 \text{ ms}^{-1}$. With these transport parameters they were able to simulate the long-term evolution of the polar fields, the formation of spiral patterns in the photosphere when observed at the poles, and the rotation of the large-scale photospheric and coronal fields. It was also suggested that the discrepancy in results between this study and DeVore *et.al.* [DeVo85] is that “the high-resolution NSOKP data show much smaller scale structures than can be reproduced by [the flux-transport equation]”.

In an attempt to extend the model to scales comparable to that of the supergranulation Wang and Sheeley [Wang94] used the flux-transport equation with the diffusive term replaced by a discrete random walk to simulate the photospheric field during sunspot cycle 21. In this model a fixed number of cells are randomly selected at each time step, all magnetic flux in each cell is moved a fixed length l in a random direction α relative to the centre of the original cell. A MWO synoptic map was used as the initial flux distribution field, and the transport parameters were taken as in previous NRL papers. It was concluded that the random walk model could not account for existence of differentially rotating, intermediate-scale magnetic structures with lifetimes of 27 days and longer, but Wang and Sheeley suggested that the simulations demonstrated how the rotation of the photospheric field may be quasi-rigid on global scales and yet strongly differential on smaller spatial scales.

2.4. Other Groups and The Flux-Transport Equation

Based on the assumption that magnetic structures provide a reliable means of determining flow speeds, a number of groups have made direct measurements of flow speeds from magnetograms.

Cross-correlation was employed to examine the short-term rotation of fields over the whole surface of the Sun by Snodgrass [Snod83]. MWO magnetograms, divided into latitude strips, were cross-correlated at increments of 1,2,3 and 4 successive days. The period covered was $15\frac{1}{2}$ years for which the digitised magnetograms were available. A standard means of summarising solar rotation profiles is by fitting them with the functional form

$$\omega(\theta) = A + B \sin^2\left(\frac{\pi}{2} - \theta\right) + C \sin^4\left(\frac{\pi}{2} - \theta\right)$$

where θ is the co-latitude, A is a “rigid” rotation rate, B and C give the “differential” rotation. Snodgrass found the day-to-day rotation of solar magnetic features to be steady over the whole surface, showing neither measurable dependence on field strength nor variation with time. Furthermore, the synodic rate for solar latitude ϕ was found to be

$$\omega(\theta) = 2.902 - 0.464 \sin^2\left(\frac{\pi}{2} - \theta\right) - 0.328 \sin^4\left(\frac{\pi}{2} - \theta\right) \mu\text{rad s}^{-1}.$$

Komm *et al.* [Kom93a] also investigated the large-scale motions of the solar surface magnetic features by analysing 689 high-resolution full-disc NSOKP daily magnetograms, using one- and two-dimensional cross correlation of analysis of consecutive day pairs. It was found that the main sidereal rotation rate of small magnetic features is best fit by $\omega(\theta) = 2.913(\pm 0.004) - 0.405(\pm 0.027) \sin^2(\pi/2 - \theta) - 0.422(\pm 0.030) \sin^4(\pi/2 - \theta) \mu\text{rad s}^{-1}$. Furthermore, Komm *et al.* showed that the large-scale motion can be divided into rotational and meridional components which

are not affected by each other [**Kom93b**], and the meridional flow is of magnitude 10ms^{-1} poleward [**Kom93c**].

Deng *et.al* [**Deng99**] made measurements of the solar rotation rate near the polar region by tracing the motion of more than 1300 magnetic elements between latitudes 55° and 85° using two sets of data (i) longitudinal magnetograms recorded using Huairou Solar Observation Station (China) videomagnetograph, and (ii) NSOKP daily full-disc magnetograms. It was deduced that

$$\omega = 2.828(\pm 0.109) - 0.453(\pm 0.246) \sin^2(\pi/2 - \theta) - 0.360(\pm 0.160) \sin^4(\pi/2 - \theta) \mu\text{rad day}^{-1}$$

where θ is latitude.

Snodgrass *et.al.* [**Snod91**], [**Snod96**] cross-correlated full-disc MWO magnetograms spaced a full solar rotation apart following the method set out in Snodgrass' 1983 paper [**Snod83**] and it was concluded that there is a constant, generally prevailing meridional motion which is perhaps poleward everywhere and varies smoothly with latitude.

By applying a new method of processing sequences of daily full-disc WSO magnetograms, Grigoryev and Latushko [**Grig92**] estimated the angular velocity of large-scale magnetic field rotation, that is, differential rotation. In this method the large-scale field structures are used as tracers, from which the differential rotation was obtained by averaging latitudinal scans of the residual velocities. They identified two possible systematic errors with this new method and concluded that further investigations with larger sets of observational data was required to validate the method. This work was followed up by Latushko [**Latu93**], [**Latu94**] in which 17 years of synoptic maps from NSOKP and MWO were divided into 69 partly overlapping subsets of length 6 rotations each with steps of 3 rotations. Then two-dimensional cross-correlations were used on 10° latitudinal belts used to determine the displacement

of the field pattern in latitude and longitude for one Carrington rotation. From this estimates were made of the drift rate and angular rate for the middle of the time interval and the centre of the latitudinal belts.

Cameron *et.al.* [**Came98**] introduced a new method for establishing the meridional flow profile that refines the DeVore *et.al.* [**DeVo87**] model of meridional flow. MWO coarse synoptic magnetic field data was averaged longitudinally for each Carrington rotation. Assuming that the motion of the solar surface magnetic field is described by the flux-transport equation, the flux-transport equation is integrated in the longitudinal direction so as to reduce the problem to one spatial dimension. This implies that only the meridional flow of the gross, or average, magnetic field can be established. Using the flux-transport equation, a least-squares fitting algorithm was implemented to determine the meridional velocity profile for a chosen diffusivity which best accounts for observed changes in the magnetic field. It was concluded that the small differences between the results could be interpreted as some measure of the error which should be associated with the velocity profile due to various assumptions which have been incorporated in the model. By comparison to other studies the results have all the essential features

- All change sign at the equator,
- All peak in latitude regions $\pm 20 - 40$ with velocities of $10ms^{-1}$
- All decay to zero at higher latitudes.

They found a parametric fit to their results expressing the solar meridional flow as $v(\phi) = 28.5 \sin^2 \phi \cos \phi$, that is, $p = 1$ and $q = 1$ which is rather different to the values $p = 99$ and $q = 0.04$ found by DeVore *et.al.* [**DeVo87**].

In studying the outer atmospheric activity of cool stars, Schrijver [**Schr01**] considered simulations of cool stars based on characteristics of the solar magnetic fields. Schrijver employed the flux transport equation to construct several series of synthetic

instantaneous maps. Each series represent a model with alternative characteristics from a standard model based on solar characteristics. These alternative characteristics included altered magnetic activity proportional to the solar magnetic activity, different meridional rates and varying maximum flux in emerging regions. From each series synoptic maps were constructed according to the procedure used at NSOKP. Histograms of flux density were derived from the synoptic maps and compared against histograms of flux density for the standard model and the other construct models. From this, simulations of the magnetic fields of cool stars similar to the Sun covering several orders of magnitude of activity were considered, and used to estimate the surface-averaged radiative losses associated with those fields.

Wilson and McIntosh [**Wils91**] presented observations of the first large-scale patterns near the sunspot minimum of 1986 (beginning of cycle 22) using synoptic maps. The flux-transport equation was numerically solved using MWO synoptic maps as initial conditions, with the data set adjusted for emergence of flux after each rotation to account for significant flux eruption which may have occurred whilst in transit on the invisible solar hemisphere. Some discrepancies between observed and simulated contour synoptic maps may be removed by local variations of the parameters of the flux-transport equation, but several qualitative differences were noted which could not be resolved in this way.

One of these qualitative differences was the development of a trans-equatorial cell identified at the beginning of cycle 22. Wilson [**Wils92**] continued simulations with the flux-transport equation using MWO synoptic maps as initial conditions to examine the relationship between the first active region of cycle 22 and this cell. It was concluded that the development of this cell is different to the diffusion-decay model of the flux-transport equation.

Continuing the investigation of the start of cycle 22, Murray and Wilson [Murr92] described changes in the polar fields using MWO synoptic maps, and compared them with simulations using flux-transport equation and based on the observed fields of Carrington rotation 1815. Once again the MWO synoptic maps were used as the initial conditions for numerically solving the flux-transport equation. It was concluded that the polar reversal was not solely due to poleward drift of decaying active region flux from below $\pm 50^\circ$ latitude but was also influenced by the emergence at high latitudes of large-scale field patterns.

Wilson and Giovannis [Wils94] investigated simulations of the reversal of the solar polar magnetic fields. The flux-transport equation for the radial component of the large-scales was solved numerically through to CR 1866 with the observed MWO synoptic magnetic field for CR 1815 taken as the initial condition. To incorporate the effect of emerging active regions, all grid values between latitude $\pm 50^\circ$ were updated after each rotation by substituting observed MWO values for the new rotation. It was concluded that something was lacking in the flux-transport equation model of the polar field reversals.

The life histories of several individual active regions were studied and compared with the evolution of the active regions found by simulations based upon the flux-transport equation by Kress *et.al.* [Kres99]. Regions which emerged early in cycle 22 were studied by using synoptic charts and daily magnetograms from NSOKP. To model the decay of the selected regions, the flux-transport equation was employed. Kress and Wilson stressed that it is not implied that all regions should decay in this way, rather, these simulations provide a reference model against which the different decay patterns may be characterised and assessed. The flux-transport equation was solved numerically to simulate the evolution of the radial field B_r , taking the observed

NSOKP synoptic magnetic field at a particular Carrington rotation as the initial condition.

The Snodgrass differential rotation model [Snod83], and the Cameron and Hopkins [Came98] meridional flow model with a maximal value of v_o at latitude 32.3° were chosen. A constant coefficient for diffusion, κ , was assumed, so that the simulations have two free parameters v_o and κ . Initial simulations used $v_o = 10 \text{ ms}^{-1}$ (Cameron and Hopkins), and $\kappa = 600 \text{ km}^2\text{s}^{-1}$ (Wang, Nash, Sheeley). In subsequent simulations the parameters were varied to best match observed decay of the region in question. For each region under investigation, the initial field was chosen to be the NSOKP synoptic map for the Carrington rotation corresponding to the onset of the decay of that region. They were evolved forward by taking repeated integration steps $\sim 3 \text{ hr}$ until the region could no longer be reliably identified in the observed maps or until it became deformed by newly emerging active regions. It was concluded that although the flux-transport equation may provide a reasonable qualitative account of the decay of many active regions, it is a simplified model which sometimes fails to describe the evolution of individual regions. These may be influenced by subsurface activity resulting in the emergence of small bipoles and phenomena related to the stability of sunspots.

Kress and Wilson continued studying simulations of the polar fields using the flux-transport equation [Kres00]. The flux-transport equation was numerically solved to simulate the evolution of the radial field, B_r , taking the observed MWO synoptic magnetic field for a particular Carrington rotation as the initial condition. To include the effect of emerging active regions in the simulations for the next and subsequent rotations, all grid values between $\pm 46^\circ$ latitude were updated after each rotation by substituting MWO observed values for this new rotation in place of the simulated values. They justified this on the basis of the Babcock-Leighton model which assumes

no large-scale flux patterns emerges at latitudes greater than 50° . Thus the evolution of simulated fields above 50° latitude reflects only the local effects of diffusion and transport of decaying active region fields from lower latitudes by meridional flow and differential rotation. It was concluded that it is possible to simulate the general features of the polar field reversals using the flux-transport equation with parameter values of order $\kappa = 600 \text{ km}^2\text{s}^{-1}$ and $v_o = 11 \text{ ms}^{-1}$. This approach was continued by Durrant *et.al.* [Durr01] using the same parameters, and gave similar results.

Supergranular convective cells appear to be randomly distributed across the non-active solar surface, so Worden and Harvey used random “attractors”¹ to model diffusion by creating an “attractor” matrix of 360×180 pixels and assigning each pixel a random attractor number between 0 and infinity. By taking the inverse of a randomly generated set of numbers uniformly distributed between 0 and 1. The attractor map values are multiplied by $\cos \theta$, where θ is latitude, in order to conserve the mean attractor value per unit area. Daily estimates of the magnetic flux distribution on the entire solar surface (instantaneous maps) are produced. Their procedure creates this map by building it up day by day using magnetograms mapped onto a latitude-longitude grid. The magnetogram for the first day yields a partial map which is then evolved using the flux-transport equation for one day. This is compared with the magnetogram for the next day and in the region of overlap the latter is used to replace the flux distribution of the evolved map. This is continued to the end of the rotation, by which time the set of partial maps combines to produce a complete map of instantaneous flux distribution corresponding to the last of the last rotation. In this procedure the flux-transport equation is being used to predict what has happened

¹“Attractors” was a term used by Harvey and Worden to define the preferred sinks of supergranular motion and is not to be confused with the attractors in non-linear analysis.

to flux on the unobservable hemisphere since it was observed earlier in the rotation, using all the information in a series of magnetograms.

Since the NRL group first formally described the magnetic field transport of the Babcock-Leighton model by the flux transport equation, a voluminous number of investigations into the evolution of the solar surface flux has been carried out. As illustrated by sections (2.3) and (2.4) the flux transport equation has played a central role in describing the flux evolution over the surface of the Sun. It has been applied ubiquitously to magnetograms and synoptic maps in these studies. The following chapter will examine whether it is an incorrect assumption that the flux-transport equation can be applied to synoptic maps.

CHAPTER 3

A Cartesian Model

As illustrated by in Chapter 2, the flux-transport equation has enjoyed a central role in a considerable number of studies of the evolution of solar surface flux since the NRL group developed it from Leighton's random-walk model with Babcock's suggested meridional flow incorporated. A major emphasis of Chapter 2 was on the type of map, magnetogram or synoptic, to which the flux-transport equation was applied in each of these studies. This Chapter examines whether it is a correct assumption that the flux-transport equation can be applied to synoptic maps by considering an analytic model constructed in a Cartesian system.

Consider one of the solar hemispheres as a Cartesian xy -plane. Let the x -axis be parallel to the equator, y -axis be parallel to a line of longitude and the z -axis be radial. This grid allows no singular points, so the model uses only a finite band of latitudes about the equator. The surface is taken to lie between $0 \leq x \leq L$. The advection part of the flux-transport equation is

$$(3.1) \quad \frac{\partial B_z}{\partial t} + \frac{\partial}{\partial x} (v_x B_z) + \frac{\partial}{\partial y} (v_y B_z) = 0$$

For the special case where the meridional flow, v_y , is constant and the differential rotation depends upon "latitude", $v_x = v_x(y)$. Then equation (3.1) becomes

$$(3.2) \quad \frac{\partial B_z}{\partial t} + v_x \frac{\partial B_z}{\partial x} + v_y \frac{\partial B_z}{\partial y} = 0.$$

3.1. The Instantaneous Map

Consider a periodic solution in time, t , and longitude, x , between 0 and L which has the form

$$B_0(x, y, t) = e^{i\omega t} e^{i\frac{2\pi n}{L}x} B(y)$$

where $2\pi/\omega$ is the period of the “cycle” and L/n is the longitudinal wavelength. The derivatives of a solution of this form are

$$\begin{aligned} \frac{\partial B_0}{\partial t} &= i\omega e^{i\omega t} e^{i\frac{2\pi n}{L}x} B(y), \\ \frac{\partial B_0}{\partial x} &= i\frac{2\pi n}{L} e^{i\omega t} e^{i\frac{2\pi n}{L}x} B(y), \\ \frac{\partial B_0}{\partial y} &= \frac{dB}{dy} e^{i\omega t} e^{i\frac{2\pi n}{L}x}. \end{aligned}$$

Therefore the solution satisfies the zero-diffusion flux-transport equation if

$$i\omega e^{i\omega t} e^{i\frac{2\pi n}{L}x} B(y) + v_x i\frac{2\pi n}{L} e^{i\omega t} e^{i\frac{2\pi n}{L}x} B(y) + v_y \frac{dB}{dy} e^{i\omega t} e^{i\frac{2\pi n}{L}x} = 0$$

which is

$$i\omega B(y) + v_x i\frac{2\pi n}{L} B(y) + v_y \frac{dB}{dy} = 0,$$

since $e^{i\omega t} \neq 0$ for all t . By letting $v_x = v_x(y)$ and $v_y = \text{constant} = \nu$ this is

$$\left(i\omega + i\frac{2\pi n}{L} v_x(y) \right) B + \nu \frac{dB}{dy} = 0.$$

Now consider specific $v_x(y)$ of the n^{th} -degree polynomial form,

$$v_x(y) = \sum_{k=0}^n a_k y^k.$$

Use integrating factors to find a solution, B , to

$$i \left(\omega + \frac{2\pi n}{L} \sum_{k=0}^n a_k y^k \right) B + \nu \frac{dB}{dy} = 0.$$

The integration factor is

$$\begin{aligned} I(y) &= \exp i \left\{ \int \left(\frac{\omega}{\nu} + \frac{2\pi n}{\nu L} \sum_{k=0}^n a_k y^k \right) dy \right\} \\ &= \exp i \left(\frac{\omega}{\nu} y + \frac{2\pi n}{\nu L} \sum_{k=0}^n \frac{1}{k+1} a_k y^{k+1} \right). \end{aligned}$$

and $B(y)$ is

$$B = A \exp \left\{ i \left(-\frac{\omega}{\nu} y - \frac{2\pi n}{\nu L} \sum_{k=0}^n \frac{1}{k+1} a_k y^{k+1} \right) \right\}.$$

In the special case where v_x is a linear function of “latitude”, $v_x(y) = a_1 y$, $a_1 \neq 0$,

$$B = A \exp \left\{ i \left(-\frac{\omega}{\nu} y - \frac{\pi n}{\nu L} a_1 y^2 \right) \right\},$$

and the radial field as a function of time is

$$B_0(x, y, t) = A \exp \left\{ i \left(\omega t + \frac{2\pi n}{L} x - \frac{\omega}{\nu} y - \frac{a_1 \pi n}{\nu L} y^2 \right) \right\}$$

which is the *instantaneous map*.

3.2. The Time-Stepped Synoptic Map

If rotation is mimicked, by allowing the “meridian” to drift in the negative x -direction at a rate $L\Omega$, then a synoptic map at τ can be created by the replacement $t = \tau + (L - x)/L\Omega$,

$$\begin{aligned} \mathcal{B}_{0_z}(x, y, \tau) &= B_0 \left(x, y, \tau + \frac{L - x}{L\Omega} \right) \\ (3.3) \quad &= A \exp \left\{ i \left(\omega \tau + \omega \frac{L - x}{L\Omega} + \frac{2\pi n}{L} x - \frac{\omega}{\nu} y - \frac{a_1 \pi n}{\nu L} y^2 \right) \right\}. \end{aligned}$$

Now, by letting $\tau = t$, substituting $\mathcal{B}_{0_z}(x, y, t)$ into the flux-transport equation, assuming $A \neq 0$,

$$\begin{aligned} (3.4) \quad \frac{\partial \mathcal{B}_{0_z}}{\partial t} + a_1 y \frac{\partial \mathcal{B}_{0_z}}{\partial x} + \nu \frac{\partial \mathcal{B}_{0_z}}{\partial y} &= \omega + a_1 y \left(\frac{2\pi n}{L} - \frac{\omega}{\Omega L} \right) + \nu \left(-\frac{\omega}{\nu} - \frac{2a_1 \pi n}{\nu L} y \right) \\ &= -\frac{a_1 \omega}{\Omega L} y, \end{aligned}$$

which is non-zero for all $y \neq 0$, assuming that $\omega, a_1, L \neq 0$. Thus this constructed synoptic map does not satisfy the flux transport equation.

3.3. The Analytic Version of the Synoptic Map

Consider an initial condition given by equation (3.3) with $\tau = 0$, that is,

$$(3.5) \quad \mathcal{B}_z(x, y, 0) = \exp \left\{ i \left(\frac{\omega}{\Omega} + \left(\frac{2\pi n}{L} - \frac{\omega}{\Omega L} \right) x - \frac{\omega}{\nu} y - \frac{a_1 \pi n}{\nu L} y^2 \right) \right\}.$$

Then the solution of

$$\frac{\partial \mathcal{B}_z}{\partial t} + a_1 y \frac{\partial \mathcal{B}_z}{\partial x} + \nu \frac{\partial \mathcal{B}_z}{\partial y} = 0$$

with the initial condition (3.5) can be determined by the method of characteristics.

Firstly, start with the following characteristic equations:

$$\frac{\partial t}{\partial \sigma} = 1, \quad \frac{\partial x}{\partial \sigma} = a_1 y, \quad \frac{\partial y}{\partial \sigma} = \nu, \quad \frac{\partial \mathcal{B}_z}{\partial \sigma} = 0.$$

Integrating the first, third and fourth of these equations,

$$t = \sigma + C_1, \quad y = \nu \sigma + C_2, \quad \mathcal{B}_z = C_3$$

are obtained and then the second characteristic equation becomes,

$$\frac{\partial x}{\partial \sigma} = a_1 \nu \sigma + a_1 C_2,$$

which by integration gives

$$x = \frac{1}{2} a_1 \nu \sigma^2 + a_1 C_2 \sigma + C_4.$$

The initial conditions are parameterised by choosing $\sigma = 0$, which gives

$$t = 0, \quad x = \gamma, \quad y = \delta, \quad \mathcal{B}_z = \exp \left\{ i \left(\frac{\omega}{\Omega} + \left(\frac{2\pi n}{L} - \frac{\omega}{\Omega L} \right) x + \left(-\frac{\omega}{\nu} y - \frac{a_1 \pi n}{\nu L} y^2 \right) \right) \right\}$$

Thus from the initial conditions and the characteristic equations

$$C_1 = 0, \quad C_2 = \delta, \quad C_3 = \mathcal{B}_z, \quad C_4 = \gamma.$$

Thus the integrated characteristic equations become

$$t = \sigma, \quad x = \frac{1}{2}a_1\nu\sigma^2 + a_1\delta\sigma + \gamma, \quad y = \nu\sigma + \delta,$$

$$\mathcal{B}_z = \exp \left\{ i \left(\frac{\omega}{\Omega} + \frac{2\pi n}{L} - \frac{\omega}{\Omega L} \gamma - \frac{\omega}{\nu} \delta - \frac{a_1\pi n}{\nu L} \delta^2 \right) \right\}.$$

By rearranging we have

$$\sigma = t, \quad \delta = y - \nu t, \quad \gamma = x - a_1 y t + \frac{1}{2} a_1 \nu t^2.$$

Hence

$$\mathcal{B}_z(x, y, t)$$

$$= \exp \left\{ i \left(\frac{\omega}{\Omega} + \left(\frac{2\pi n}{L} - \frac{\omega}{\Omega L} \right) \left(x - a_1 y t + \frac{1}{2} a_1 \nu t^2 \right) - \frac{\omega}{\nu} (y - \nu t) - \frac{a_1 \pi n}{\nu L} (y - \nu t)^2 \right) \right\}$$

But this is no longer periodic in either time or longitude. Hence synoptic maps modelled using the flux-transport equation which describes the evolution of instantaneous maps would not reproduce the actual maps (3.3).

Now consider trying to determine the velocity fields by matching the actual synoptic maps with models of synoptic evolution using the flux transport equation, that is, by forcing the synoptic map (3.3) to satisfy an equation of the form (3.1) or (3.2). If a constant $v_y = \nu$ is maintained, then (3.3) will satisfy (3.1) if

$$v_x = \frac{a_1 y}{1 - (\omega/2\pi n \Omega)}.$$

Alternatively, if $v_x = a_1 y$ is maintained, then (3.3) will satisfy (3.2) if

$$v_y = \nu \left(\frac{L(\omega/2\pi n) + (1 - (\omega/2\pi n \Omega)) a_1 y}{L(\omega/2\pi n) + a_1 y} \right).$$

This is inconsistent since (3.1) leads to (3.2) only if v_y is independent of y . However, it does demonstrate that there are enough parameters in the flux-transport equation for the synoptic transport to be mimicked by a careful choice of these parameters. But

these parameters no longer measure the true flow speeds that describe the evolution of the instantaneous maps.

The model has an exactly periodic magnetic variation at any point of the surface of period $2\pi/\omega$. This is called the “cycle” in analogy to the quasi-periodic solar magnetic cycle. The only time dependence in this model is through this “cycle” variation with rate ω/Ω relative to the rotation rate. As $\omega/\Omega \rightarrow 0$, $v_y \rightarrow \nu$, that is, the derived flow speeds tend to the true values. The discrepancy between the true and derived values is of order ω/Ω , which is the ratio of the rotation period to the “cycle” period, and in the Sun this would be about 1/300. Thus the discrepancies would be rather small. However, in the Sun, the flux distribution is not close to a steady state, varying only slowly with a 22 year cycle. The injection of new flux varies in time and space, the time scale for the development of active regions is of the order of a rotation time. Therefore, in this case, the quantity ω/Ω will be of the order of unity and the discrepancies between true and derived values will be marked.

Chapter 3 has shown, by the use of a simple analytic model in a Cartesian system, that discrepancies arise when the flux-transport equation is applied to synoptic maps. Attempting to simulate synoptic maps using the flux-transport equation with given transport parameters fails to reproduce actual synoptic maps, and transport parameters derived from applying the flux-transport equation to synoptic maps are in error with the true transport parameters. To be more precise about the inconsistencies which arise due to the application of the flux-transport equation to synoptic maps, a more exact model of the solar case needs to be examined. Thus Chapter 4 will consider a spherical geometry model in which the underlying reasons behind these discrepancies will become more apparent.

CHAPTER 4

The Synoptic Transport Equation

The analytic Cartesian model presented in Chapter 3 though simple in nature offered an excellent illustration that the flux transport equation cannot be used in conjunction with synoptic observations. In this chapter, the unique equation which describes the temporal evolution of a synoptic map is derived; this is termed the synoptic transport equation. Since it is based upon the evolution of instantaneous maps according to the flux-transport equation, the flux-transport equation is described in spherical geometry firstly. Then the transformation from the instantaneous map to the synoptic map is used to produce the synoptic transport equation.

4.1. The flux-transport equation

The evolution of the magnetic field \mathbf{B} is governed by the three dimensional induction equation

$$(4.1) \quad \frac{\partial \mathbf{B}}{\partial t} = \nabla \times (\mathbf{v} \times \mathbf{B}) + \eta \nabla^2 \mathbf{B}$$

where η is the magnetic diffusivity of the plasma. For a kinematic model, the velocity field \mathbf{v} is specified and then the induction equation together with Maxwell's equation

$$(4.2) \quad \nabla \cdot \mathbf{B} = 0$$

determines how the field evolves. In terms of spherical-polar co-ordinates, where ϕ is latitude and θ is co-latitude, the radial component of the induction equation (4.1) is

$$\begin{aligned}
 \frac{\partial B_r}{\partial t} &= \frac{1}{r \sin \theta} \frac{\partial}{\partial \theta} ((\sin \theta)(v_r B_\theta - v_\theta B_r)) - \frac{1}{r \sin \theta} \frac{\partial}{\partial \phi} ((v_\phi B_r - v_r B_\phi)) \\
 (4.3) \quad &+ \eta \frac{\partial}{\partial r} \left(\frac{1}{r^2} \frac{\partial}{\partial r} (r^2 B_r) \right) + \frac{\eta}{r^2 \sin \theta} \frac{\partial}{\partial \theta} \left(\sin \theta \frac{\partial B_r}{\partial \theta} \right) \\
 &+ \frac{\eta}{r^2 \sin^2 \theta} \frac{\partial^2 B_r}{\partial \phi^2} - \frac{2\eta}{r^2 \sin \theta} \frac{\partial}{\partial \theta} (\sin \theta B_\theta) - \frac{2\eta}{r^2 \sin \theta} \frac{\partial B_\phi}{\partial \phi}
 \end{aligned}$$

and Maxwell's equation (4.2) becomes

$$(4.4) \quad \frac{1}{r^2} \frac{\partial}{\partial r} (r^2 B_r) + \frac{1}{r \sin \theta} \frac{\partial}{\partial \theta} (\sin \theta B_\theta) + \frac{1}{r \sin \theta} \frac{\partial B_\phi}{\partial \phi} = 0$$

Since magnetograms have a finite spatial resolution, explicit averaging in the horizontal and vertical directions is required. The smoothing in the vertical direction due to the process of radiative transfer along the line-of-sight is ignored since the scale height of the atmosphere is small in comparison to the size of the horizontal spatial resolution element. In order to apply the horizontal smoothing, a local Cartesian co-ordinate system (x, y, z) is invoked in which x is in the positive θ -direction (equatorward), y is in the positive ϕ -direction (Eastward) and z is in the positive r -direction (radial).

If the filter is applied uniformly, by applying a convolution with a function $f(x - x', y - y')$ and utilising the property that f vanishes outside a small finite domain, then the terms linear in v and B turn into linear terms in \bar{v} and \bar{B} . The overline indicates a spatially averaged quantity, and the derivatives are as follows

$$\begin{aligned}
 \int f(x - x', y - y') \frac{\partial X}{\partial t} dx' dy' X(x', y') dx' dy' &= \frac{\partial}{\partial t} \int f(x - x', y - y') X(x', y') dx' dy' \\
 &= \frac{\partial \bar{X}}{\partial t},
 \end{aligned}$$

and similarly for the z -derivative, and

$$\begin{aligned}
\int f(x-x', y-y') \frac{\partial X}{\partial x} dx' dy' &= - \int X(x', y') \frac{\partial f}{\partial x'} dx' dy' \\
&= \int X(x', y') \frac{\partial f}{\partial x} dx' dy' \\
&= \frac{\partial}{\partial x} \int X(x', y') f(x-x', y-y') dx' dy' \\
&= \frac{\partial \bar{X}}{\partial x},
\end{aligned}$$

and similarly for the y -derivative. For the moment the quadratic terms cannot be expressed as products of spatially averaged quantities. Thus after applying the spatial filter, the radial component of the induction equation (4.3) in terms of averaged quantities is

$$\begin{aligned}
(4.5) \quad \frac{\partial \bar{B}_r}{\partial t} &= - \frac{1}{r \sin \theta} \frac{\partial}{\partial \theta} (\sin \theta (\overline{v_\theta B_r})) - \frac{1}{r \sin \theta} \frac{\partial}{\partial \phi} (\overline{v_\phi B_r}) \\
&\quad - \frac{1}{r \sin \theta} \frac{\partial}{\partial \theta} (\sin \theta (\overline{v_r B_\theta})) + \frac{1}{r \sin \theta} \frac{\partial}{\partial \phi} (\overline{v_r B_\phi}) \\
&\quad + \eta \frac{\partial}{\partial r} \left(\frac{1}{r^2} \frac{\partial}{\partial r} (r^2 \bar{B}_r) \right) + \frac{\eta}{r^2 \sin \theta} \frac{\partial}{\partial \theta} \left(\sin \theta \frac{\partial \bar{B}_r}{\partial \theta} \right) + \frac{\eta}{r^2 \sin^2 \theta} \frac{\partial^2 \bar{B}_r}{\partial \phi^2} \\
&\quad - \frac{2\eta}{r^2 \sin \theta} \frac{\partial}{\partial \theta} (\sin \theta \bar{B}_\phi) - \frac{2\eta}{r^2 \sin \theta} \frac{\partial \bar{B}_\phi}{\partial \phi},
\end{aligned}$$

and Maxwell's equation (4.4) becomes

$$(4.6) \quad \frac{1}{r^2} \frac{\partial}{\partial r} (r^2 \bar{B}_r) + \frac{1}{r \sin \theta} \frac{\partial}{\partial \theta} (\sin \theta \bar{B}_\theta) + \frac{1}{r \sin \theta} \frac{\partial \bar{B}_\phi}{\partial \phi} = 0.$$

At the surface $r = R$, thus

$$\begin{aligned}
(4.7) \quad \frac{\partial \bar{B}_r}{\partial t} = & -\frac{1}{R \sin \theta} \frac{\partial}{\partial \theta} (\sin \theta (\overline{v_\theta B_r})) - \frac{1}{R \sin \theta} \frac{\partial}{\partial \phi} (\overline{v_\phi B_r}) \\
& - \frac{1}{R \sin \theta} \frac{\partial}{\partial \theta} (\sin \theta (\overline{v_r B_\theta})) + \frac{1}{R \sin \theta} \frac{\partial}{\partial \phi} (\overline{v_r B_\phi}) \\
& + \eta \frac{\partial}{\partial r} \left(\frac{1}{r^2} \frac{\partial}{\partial r} (r^2 \bar{B}_r) \right) \Big|_{r=R} + \frac{\eta}{R^2 \sin \theta} \frac{\partial}{\partial \theta} \left(\sin \theta \frac{\partial \bar{B}_r}{\partial \theta} \right) + \frac{\eta}{R^2 \sin^2 \theta} \frac{\partial^2 \bar{B}_r}{\partial \phi^2} \\
& - \frac{2\eta}{R^2 \sin \theta} \frac{\partial}{\partial \theta} (\sin \theta \bar{B}_\phi) - \frac{2\eta}{R^2 \sin \theta} \frac{\partial \bar{B}_\phi}{\partial \phi},
\end{aligned}$$

and

$$(4.8) \quad \frac{1}{r^2} \frac{\partial}{\partial r} (r^2 \bar{B}_r) \Big|_{r=R} + \frac{1}{R \sin \theta} \frac{\partial}{\partial \theta} (\sin \theta \bar{B}_\theta) + \frac{1}{R \sin \theta} \frac{\partial \bar{B}_\phi}{\partial \phi} = 0.$$

where all quantities with overlines are evaluated at $r = R$.

The quadratic quantities must be evaluated in the local co-ordinate system, for example,

$$\overline{v_\theta B_r}(x, y, R) = \iint v_x(x', y', R) B_z(x', y', R) f(x - x', y - y') dx' dy',$$

using a model for the unresolved fields. Analogous evaluations as *ensemble* averages have been made in the context of dynamo theory for various models of the small-scale fields. All assume isotropy¹ and lead to the approximate form

$$\nabla \times (\overline{\mathbf{v} \times \mathbf{B}}) = \nabla \times (\bar{\mathbf{v}} \times \bar{\mathbf{B}}) + \eta_t \nabla^2 \bar{\mathbf{B}},$$

where η_t is a ‘turbulent’ magnetic diffusivity which is isotropic and is estimated as ℓ^2/τ for typical length, ℓ , and time, τ , scales over which the small-scale fields are correlated. This model is the basis of the discussion in DeVore *et al.* [DeVo84], and outlined here in section 2.3.1. In the context given here, this treatment is not appropriate because the small-scale fields are not isotropic close to the surface where equation (4.7) is to be applied. The magnetic induction is primarily radial and the

¹This suppresses the α -effect in dynamo theory which is due to cyclonic motion

velocities are primarily horizontal. However, the properties of the unresolved (small-scale) velocity fields are expected to be isotropic and uniform over the horizontal resolution element. Hence, using a derivation by Durrant (unpublished), consider the following treatment.

Consider the component $\overline{v_x B_z}$ and suppose that $v_x = \bar{v}_x + v$ where v is a random small-scale velocity field with probability density function $P(v)$ and which carries the field B_z without change for a time τ over a distance $\ell = v\tau$ before ceasing to advect the field. Then

$$\begin{aligned}\overline{v_x B_z} &= \bar{v}_x \bar{B}_z + \overline{v B_z} \\ &= \bar{v}_x \bar{B}_z + \iint v(x', y') B_z(x', y') f(x - x', y - y') dx' dy'.\end{aligned}$$

Since the properties of v are assumed uniform, that is, independent of y' , the integral can be evaluated in one dimension

$$\iint v(x', y') B_z(x', y') f(x - x', y - y') dx' dy' \equiv \int v(x') B_z(x', y) f(x - x') dx',$$

where quantities on the right-hand side are considered to be averages over y' . The spatial average is replaced by the statistical average of the field B_z arriving at x with velocity v ,

$$\int v(x') B_z(x', y) f(x - x') dx' = \int dv v P(v) \int Q\langle x' | v \rangle \bar{B}_z(x') dx'$$

where $Q\langle x' | v \rangle$ is the conditional probability that the flow originates from x' given a flow speed of v and $\bar{B}_z(x')$ is the average field at x' .

When $v > 0$, $\langle x | v \rangle = 0$ for $x - x' > 0$ and $x' - x < -v\tau$, and $Q\langle x | v \rangle = C$ is a constant for $-v\tau < x' - x < 0$. Since $\int_0^\infty Q\langle x' | v \rangle dx' = 1$, $C = 1/v\tau$.

When $v < 0$, $Q\langle x' | v \rangle = 1/|v|\tau$ for $0 < x' - x < |v|\tau$.

Hence

$$\begin{aligned}
(4.9) \quad & \int dv v P(v) \int Q\langle x' | v \rangle B_z(x') dx' \\
&= \frac{1}{\tau} \int_0^\infty dv P(v) \int_{x-v\tau}^x \bar{B}_z(x') dx' - \frac{1}{\tau} \int_{-\infty}^0 dv P(v) \int_x^{x-v\tau} \bar{B}_z(x') dx' \\
&\simeq \frac{1}{\tau} \int_{x-v\tau}^x \left(\bar{B}_z(x) + \frac{\partial \bar{B}_z}{\partial x}(x' - x) \right) dx' \\
&\quad - \frac{1}{\tau} \int_{-\infty}^0 dv P(v) \int_x^{x-v\tau} \left(\bar{B}_z(x) + \frac{\partial \bar{B}_z}{\partial x}(x' - x) \right) dx' \\
&= \frac{1}{\tau} \int_0^\infty dv P(v) \left(v\tau \bar{B}_z(x) - \frac{v^2\tau^2}{2} \frac{\partial \bar{B}_z}{\partial x} \right) \\
&\quad - \int_{-\infty}^0 dv P(v) \left(-v\tau \bar{B}_z(x) + \frac{v^2\tau^2}{2} \frac{\partial \bar{B}_z}{\partial x} \right) \\
&= \bar{B}_z(x) \int_{-\infty}^\infty v P(v) dv - \frac{\tau}{2} \frac{\partial \bar{B}_z}{\partial x} \int_{-\infty}^\infty v^2 P(v) dv.
\end{aligned}$$

The first integral on the right hand side vanishes since it now does not contain the mean flow \bar{v}_x . The second integral is the mean-square velocity, say v_t^2 . Thus

$$\int dv v P(v) \int Q\langle x' | v \rangle \bar{B}_z(x') dx' \simeq -\frac{v_t^2\tau}{2} \frac{\partial \bar{B}_z}{\partial x}.$$

The quantity $v_t^2\tau/2 = \ell^2/2\tau$, where ℓ is the root-mean-square distance travelled, is now defined to be the turbulent magnetic diffusivity η_t . Hence, in terms of the local Cartesian co-ordinates,

$$\overline{v_\theta B_r}(x, y, R) = \bar{v}_x \bar{B}_z - \eta_t \frac{\partial \bar{B}_z}{\partial x}$$

and, due to isotropy

$$\overline{v_\phi B_r}(x, y, R) = \bar{v}_y \bar{B}_z - \eta_t \frac{\partial \bar{B}_z}{\partial y}.$$

Substituting into equation (4.7) gives

$$\begin{aligned}
(4.10) \quad \frac{\partial \bar{B}_r}{\partial t} &= -\frac{1}{R \sin \theta} \frac{\partial}{\partial \theta} (\sin \theta (\bar{v}_\theta \bar{B}_r)) - \frac{1}{R \sin \theta} \frac{\partial}{\partial \phi} (\bar{v}_\phi \bar{B}_r) \\
&+ \frac{1}{R^2 \sin \theta} \frac{\partial}{\partial \theta} \left(\eta_t \sin \theta \frac{\partial \bar{B}_r}{\partial \theta} \right) + \frac{1}{R^2 \sin^2 \theta} \frac{\partial}{\partial \phi} \left(\eta_t \frac{\partial \bar{B}_r}{\partial \phi} \right) \\
&+ \frac{1}{R \sin \theta} \frac{\partial}{\partial \theta} (\sin \theta (\overline{v_r B_\theta})) + \frac{1}{R \sin \theta} \frac{\partial}{\partial \phi} (\overline{v_r B_\phi}) \\
&+ \eta \frac{\partial}{\partial r} \left(\frac{1}{r^2} \frac{\partial}{\partial r} (r^2 \bar{B}_r) \right) \Big|_{r=R} - \frac{2\eta}{R^2 \sin \theta} \frac{\partial}{\partial \theta} (\sin \theta \bar{B}_\theta) - \frac{2\eta}{R^2 \sin \theta} \frac{\partial \bar{B}_\phi}{\partial \phi} \\
&+ \frac{\eta}{R^2 \sin \theta} \frac{\partial}{\partial \theta} \left(\sin \theta \frac{\partial \bar{B}_r}{\partial \theta} \right) + \frac{\eta}{R^2 \sin^2 \theta} \frac{\partial^2 \bar{B}_r}{\partial \phi^2}.
\end{aligned}$$

Here η_t is allowed to vary explicitly across the surface. Since the molecular resistivity in the solar atmosphere is negligible, equation (4.10) becomes

$$\begin{aligned}
(4.11) \quad \frac{\partial \bar{B}_r}{\partial t} &= -\frac{1}{R \sin \theta} \frac{\partial}{\partial \theta} (\sin \theta (\bar{v}_\theta \bar{B}_r)) - \frac{1}{R \sin \theta} \frac{\partial}{\partial \phi} (\bar{v}_\phi \bar{B}_r) \\
&+ \frac{1}{R^2 \sin \theta} \frac{\partial}{\partial \theta} \left(\eta_t \sin \theta \frac{\partial \bar{B}_r}{\partial \theta} \right) + \frac{1}{R^2 \sin^2 \theta} \frac{\partial}{\partial \phi} \left(\eta_t \frac{\partial \bar{B}_r}{\partial \phi} \right) \\
&+ \frac{1}{R \sin \theta} \frac{\partial}{\partial \theta} (\sin \theta (\overline{v_r B_\theta})) + \frac{1}{R \sin \theta} \frac{\partial}{\partial \phi} (\overline{v_r B_\phi}).
\end{aligned}$$

The last two terms in equation (4.11) act as sources and sinks for the averaged radial field and cannot be specified arbitrarily since Maxwell's equation (4.8) must also be satisfied. These source and sink terms were dropped in the form used by the NRL group, and only this simplified form will be treated in what follows; the reason for this will be shown in section (4.4). The resulting equation involves only the spatially averaged radial field \bar{B}_r , and spatially averaged properties of the horizontal field \bar{v}_θ , \bar{v}_ϕ and η_t , and was written in vector form by Leighton [**Leig64**] as

$$\frac{\partial \bar{B}_r}{\partial t} = -\nabla_{\mathbf{s}} \cdot (\bar{B}_r \bar{\mathbf{v}}_{\mathbf{s}}) + \eta \nabla_{\mathbf{s}}^2 \bar{B}_r,$$

the subscripts \mathbf{s} denoting operators and vectors on the spherical surface. This is the flux-transport equation.

4.2. Synoptic Maps

The *synoptic map* is constructed from daily instantaneous maps $\bar{B}_r(\lambda, \phi, t)$ of the ‘radial field’ as a function of heliographic latitude, λ , and longitude, ϕ , by selecting the values near the meridian. As seen from Earth, the zero longitude advances at the synodic Carrington rotation rate of $\Omega = 2.66625 \mu\text{rad s}^{-1}$, thus the longitude of the meridian decreases as this rate. Therefore by measuring time, t , from the beginning of a rotation, $\phi = 360^\circ$, the synoptic map can be considered to be a map of flux as a function of λ and either ϕ or t ,

$$(4.12) \quad \mathcal{B}_r(\lambda, \phi) = \bar{B}_r(\lambda, \phi, (360^\circ - \phi)/\Omega),$$

or

$$(4.13) \quad \mathcal{B}_r(\lambda, t) = \bar{B}_r(\lambda, 360^\circ - \Omega t, t).$$

A third alternative is to generalise the synoptic map to being one of a set of notional maps shifted by an arbitrary time interval, that is, as seen by other ‘Earths’ at successive points around the Sun,

$$(4.14) \quad \mathcal{B}_r(\lambda, \phi, \tau) = \bar{B}_r(\lambda, \phi, \tau + (360^\circ - \phi)/\Omega).$$

The variable τ has dimension and units of time. At $\tau = 0$ the synoptic map in definition (4.12) is obtained. When $\tau = 2\pi/\Omega$ one rotation has passed, therefore (4.14) produces the synoptic map for the next Carrington rotation.

4.3. Evolution of Synoptic Maps

The more convenient polar co-ordinates are reverted to for the following where $\theta = \pi/2 - \lambda$ is colatitude. If \bar{B}_r is governed by a flux-transport equation which neglects sources and sinks, with uniform magnetic diffusivity, latitude-dependent meridional

flow $\bar{v}_\theta = v_{mf}(\theta)$ and latitude-dependent differential rotation $\bar{v}_\phi = v_{dr}(\theta)$, then

$$(4.15) \quad \begin{aligned} \frac{\partial \bar{B}_r}{\partial t} + \frac{1}{R \sin \theta} \frac{\partial}{\partial \theta} (\sin \theta v_{mf}(\theta) \bar{B}_r) + \frac{v_{dr}(\theta)}{R \sin \theta} \frac{\partial \bar{B}_r}{\partial \phi} \\ - \frac{\eta}{R^2 \sin \theta} \frac{\partial}{\partial \theta} \left(\sin \theta \frac{\partial \bar{B}_r}{\partial \theta} \right) - \frac{\eta}{R^2 \sin^2 \theta} \frac{\partial^2 \bar{B}_r}{\partial \phi^2} = 0. \end{aligned}$$

The second definition (4.13) of the synoptic map will then satisfy

$$(4.16) \quad \begin{aligned} \frac{\partial \mathcal{B}_r}{\partial t} + \frac{1}{R \sin \theta} \frac{\partial}{\partial \theta} (\sin \theta v_{mf}(\theta) \mathcal{B}_r) - \frac{\eta}{R^2 \sin \theta} \frac{\partial}{\partial \theta} \left(\sin \theta \frac{\partial \mathcal{B}_r}{\partial \theta} \right) \\ + \left(\Omega - \frac{v_{dr}(\theta)}{R \sin \theta} \right) \frac{\partial \mathcal{B}_r}{\partial \phi} \Big|_{\phi=360^\circ - \Omega t} + \frac{\eta}{R^2 \sin^2 \theta} \frac{\partial^2 \mathcal{B}_r}{\partial \phi^2} \Big|_{\phi=360^\circ - \Omega t}, \end{aligned}$$

where $\frac{\partial \mathcal{B}_r}{\partial \phi}$ and $\frac{\partial^2 \mathcal{B}_r}{\partial \phi^2}$ are meridional values of the ϕ -derivatives of the *instantaneous* map \bar{B}_r and therefore are functions of θ and t . These terms act as *source* terms for the evolution of \mathcal{B}_r . The synoptic map gives no information on these derivatives since the only available derivative,

$$\frac{\partial \mathcal{B}_r}{\partial t} = \frac{\partial \bar{B}_r}{\partial t} - \Omega \frac{\partial \bar{B}_r}{\partial \phi}$$

does not separate the time and longitudinal variations of the instantaneous map.

However, this can be overcome by using the third definition of the synoptic map (4.14), which will satisfy

$$(4.17) \quad \begin{aligned} \frac{\partial \mathcal{B}_r}{\partial \tau} + \frac{1}{R \sin \theta} \frac{\partial}{\partial \theta} (\sin \theta v_{mf}(\theta) \mathcal{B}_r) + \frac{v_{dr}(\theta)}{R \sin \theta} \frac{\partial \mathcal{B}_r}{\partial \phi} \\ - \frac{\eta}{R^2 \sin \theta} \frac{\partial}{\partial \theta} \left(\sin \theta \frac{\partial \mathcal{B}_r}{\partial \theta} \right) - \frac{\eta}{R^2 \sin^2 \theta} \frac{\partial^2 \mathcal{B}_r}{\partial \phi^2} \\ = -\frac{v_{dr}(\theta)}{\Omega R \sin \theta} \frac{\partial \mathcal{B}_r}{\partial \tau} + \frac{2\eta}{\Omega R^2 \sin^2 \theta} \frac{\partial^2 \mathcal{B}_r}{\partial \tau \partial \phi} + \frac{\eta}{\Omega^2 R^2 \sin^2 \theta} \frac{\partial^2 \mathcal{B}_r}{\partial \tau^2}. \end{aligned}$$

4.4. The Synoptic Transport Equation

Equation (4.17) is the *synoptic transport equation*, a homogeneous equation for the evolution of \mathcal{B}_r . The left-hand side of the synoptic transport equation is the original flux-transport equation applied to the synoptic quantities and the right-hand

side collects the additional terms which arise from the transformation. In previous studies, it has been assumed that the original flux transport equation can be applied to synoptic maps by implicitly neglecting the transformation terms.

The first of these transformation terms

$$-\frac{v_{dr}(\theta)}{\Omega R \sin \theta} \frac{\partial \mathcal{B}}{\partial \tau}$$

modifies the time step in a latitude-dependent manner. This changes the amount of advection and diffusion undergone in a given $d\tau$ in a way which depends on the magnitude and sign of the differential rotation. Physically the effect is due to the fact that a point on the surface at a given latitude will return to the meridian after a different time for each latitude. In the solar case, the higher latitudes rotate more slowly. Thus a high latitude point on the surface takes longer to return to the meridian than an equatorial point. Therefore the synoptic map will show display larger motion and greater diffusion at higher latitudes than the instantaneous map.

The last two terms

$$\frac{2\eta}{\Omega R^2 \sin^2 \theta} \frac{\partial^2 \mathcal{B}_r}{\partial \tau \partial \phi}, \quad \frac{\eta}{\Omega^2 R^2 \sin^2 \theta} \frac{\partial^2 \mathcal{B}_r}{\partial \tau^2}$$

involving temporal derivatives can be considered as source terms. Compared with the diffusion term in ϕ , they have magnitudes

$$1 : 2 \left(\frac{\Delta \phi}{\Omega \Delta \tau} \right) : \left(\frac{\Delta \phi}{\Omega \Delta \tau} \right)^2$$

where $\Delta \phi$ and $\Delta \tau$ are the typical scales over which \mathcal{B}_r varies in longitude and time. Diffusion is most important at the poles where new cycle flux mingles and eventually eliminates old cycle flux. The appropriate scales are those of the large-scale flux features of alternating polarity at high latitudes. Therefore the longitude scale is of the order of the length of a radian and the time scale is of the length of the solar cycle. The ratios are of the order ϵ and ϵ^2 where $\epsilon \approx 1/300$, the ratio of the rotation

period to the cycle period. Hence these two terms are small correction terms, a fact confirmed in the simplified model of the solar cycle described in the following chapter.

The synoptic transport equation in spherical geometry (4.17) can be written in a more useful form by introducing the function

$$(4.18) \quad f(\theta) = \frac{1}{1 + v_{dr}(\theta)/(\Omega R \sin \theta)}.$$

The differential rotation is given in terms of the surface differential angular velocity $\omega(\theta)$ by

$$v_{dr} = R \sin \theta (\omega(\theta) - \omega(74^\circ)).$$

The zero longitude rotates at the sidereal Carrington rate, $\omega(74^\circ) \approx 2.86485 \mu\text{rad s}^{-1}$ corresponding to a period of 25.38 days. Therefore f and the derivative of f depend upon the ratio of the differential rotation to the absolute rotation

$$f(\theta) = \frac{\Omega}{\Omega + \omega(\theta) - \omega(74^\circ)} \quad \text{and} \quad f' = -\frac{\Omega \omega'(\theta)}{(\Omega - \omega(74^\circ) + \omega(\theta))^2},$$

where the prime denotes differentiation with respect to θ .

Firstly, collecting the $\partial \mathcal{B}_r / \partial \tau$ terms in the synoptic transport equation

$$(4.19) \quad \begin{aligned} & \left(1 + \frac{v_{dr}(\theta)}{\Omega R \sin \theta}\right) \frac{\partial \mathcal{B}_r}{\partial \tau} + \frac{1}{R \sin \theta} \frac{\partial}{\partial \theta} (\sin \theta v_{mf}(\theta) \mathcal{B}_r) + \frac{v_{dr}(\theta)}{R \sin \theta} \frac{\partial \mathcal{B}_r}{\partial \phi} \\ & - \frac{\eta}{R^2 \sin \theta} \frac{\partial}{\partial \theta} \left(\sin \theta \frac{\partial \mathcal{B}_r}{\partial \theta} \right) - \frac{\eta}{R^2 \sin^2 \theta} \frac{\partial^2 \mathcal{B}_r}{\partial \phi^2} \\ & = \frac{2\eta}{\Omega R^2 \sin^2 \theta} \frac{\partial^2 \mathcal{B}_r}{\partial \tau \partial \phi} + \frac{\eta}{\Omega^2 R^2 \sin^2 \theta} \frac{\partial^2 \mathcal{B}_r}{\partial \tau^2}, \end{aligned}$$

then setting the coefficient of $\partial\mathcal{B}_r/\partial\tau$ to unity by multiplying through by $\Omega R \sin \theta / (\Omega R \sin \theta + v_{dr})$, the synoptic transport equation becomes

$$\begin{aligned}
(4.20) \quad & \frac{\partial\mathcal{B}_r}{\partial\tau} + \frac{f(\theta)}{R \sin \theta} \frac{\partial}{\partial\theta} (\sin \theta v_{mf}(\theta) \mathcal{B}_r) + \frac{v_{dr}(\theta) f(\theta)}{R \sin \theta} \frac{\partial\mathcal{B}_r}{\partial\phi} \\
& - \frac{\eta f(\theta)}{R^2 \sin \theta} \frac{\partial}{\partial\theta} \left(\sin \theta \frac{\partial\mathcal{B}_r}{\partial\theta} \right) - \frac{\eta f(\theta)}{R^2 \sin^2 \theta} \frac{\partial^2\mathcal{B}_r}{\partial\phi^2} \\
& = \frac{2\eta f(\theta)}{\Omega R^2 \sin^2 \theta} \frac{\partial^2\mathcal{B}_r}{\partial\tau\partial\phi} + \frac{\eta f(\theta)}{\Omega^2 R^2 \sin^2 \theta} \frac{\partial^2\mathcal{B}_r}{\partial\phi^2},
\end{aligned}$$

or, in conservative form

$$\begin{aligned}
(4.21) \quad & \frac{\partial\mathcal{B}_r}{\partial\tau} + \frac{1}{\sin \theta} \frac{\partial}{\partial\theta} \left(\sin \theta \left(\frac{f(\theta) v_{mf}(\theta)}{R} \right) \mathcal{B}_r \right) + \frac{1}{\sin \theta} \frac{\partial}{\partial\phi} \left(\left(\frac{f(\theta) v_{dr}(\theta)}{R} \right) \mathcal{B}_r \right) \\
& - \frac{\eta f(\theta)}{R^2 \sin \theta} \frac{\partial}{\partial\theta} \left(\sin \theta \frac{\partial\mathcal{B}_r}{\partial\theta} \right) - \frac{\eta f(\theta)}{R^2 \sin^2 \theta} \frac{\partial^2\mathcal{B}_r}{\partial\phi^2} \\
& = \frac{f'(\theta) v_{mf}(\theta) \mathcal{B}_r}{R} + \frac{2\eta f(\theta)}{\Omega R^2 \sin^2 \theta} \frac{\partial}{\partial\phi} \left(\frac{\partial\mathcal{B}_r}{\partial\tau} \right) + \frac{\eta f(\theta)}{\Omega^2 R^2 \sin^2 \theta} \frac{\partial^2\mathcal{B}_r}{\partial\tau^2}.
\end{aligned}$$

In a rigid body, the functions are $f = 1$ and $f' = 0$, and the synoptic transport and the flux-transport equation are identical. However, in the Sun the function $f(\theta)$ varies from approximately 1 at the equator to 1.40 at the poles (see Figure 7.1) according to Snodgrass' differential rotation model [**Snod83**]. Therefore the factor $f(\theta)$ increases the effective differential rotation and meridional flow rates. If the diffusivity is constant in the flux transport equation then the effective diffusion is increased by $f(\theta)$ and becomes latitude dependent in the synoptic transport equation.

To recapitulate, the synoptic transport equation differs from the flux transport equation by having modified transport processes. Both advection and diffusion are changed in a latitude-dependent manner via the function $f(\theta)$. The origin of these effects lies in the fact that points on the surface at high latitudes take longer to return to the meridian than points in the equatorial region. Hence the synoptic transport equation will display larger motion and greater diffusion at higher latitudes than the

instantaneous map. Note that in the solar case, $f \geq 1$, so that the synoptic transport equation never becomes singular.

CHAPTER 5

Implementation of the Synoptic Transport Equation

Chapter 3 illustrated that the flux-transport equation could not be used in conjunction with synoptic maps to examine solar cycle features. This led to the derivation in Chapter 4 of a unique equation, the synoptic transport equation, which could be applied to synoptic maps. It is not possible to determine an analytic solution of the spherical form of the synoptic transport equation. Therefore in this chapter a finite difference scheme is described and applied to a synthetic solar model.

5.1. Numerical Implementation of the Synoptic Transport Equation

Given the analysis in Section 4.4, the last two terms of equation (4.20) were numerically tested and confirmed to be small correction terms. Hereafter the subsequent modelling utilises the simpler synoptic transport equation

$$(5.1) \quad \begin{aligned} \frac{\partial \mathcal{B}_r}{\partial t} + \frac{f(\theta)}{R \sin \theta} \frac{\partial}{\partial \theta} (\sin \theta v_{mf}(\theta) \mathcal{B}_r) + \frac{v_{dr}(\theta) f(\theta)}{R \sin \theta} \frac{\partial \mathcal{B}}{\partial \phi} \\ - \frac{\eta f(\theta)}{R^2 \sin \theta} \frac{\partial}{\partial \theta} \left(\sin \theta \frac{\partial \mathcal{B}_r}{\partial \theta} \right) - \frac{\eta f(\theta)}{R^2 \sin^2 \theta} \frac{\partial^2 \mathcal{B}_r}{\partial \phi^2} = 0. \end{aligned}$$

The numerical scheme utilises second order finite-difference equations and is based on a Fortran subroutine ETBFCT, developed by J.R.Boris in 1975 [**Bori76**].

A number of points in the implementation of the synoptic transport equation scheme are of significance:

- *Grids.* For the purposes of this computational scheme a 180×360 latitude-longitude grid with equal 1° spacings was used. This grid is converted to a spherical grid to perform the longitude sweep calculations and then is

converted back to the Cartesian grid for the latitude sweeps. In the spherical grid, the longitude grid points are equidistant in angle, therefore the linear distance between them scales as $\sin \theta$, decreasing markedly toward the poles. This is undesirable since the uniform diffusivity will tend to enforce a uniform linear scale, not a uniform angular scale. Furthermore, the diffusion time across a cell of width Δx is dictated by the stability condition

$$\frac{\kappa \Delta t}{(\Delta x)^2} \leq 1$$

which restricts the maximum of allowed time steps Δt . Also, the Courant condition

$$\frac{|v| \Delta t}{\Delta x} \leq 1$$

demands that time steps Δt are not too large to present the communication of information between neighbouring grid points. It is an implication of both conditions that the time steps in the polar latitudes become very small. Hence a reduced grid was generated in which linear intervals were approximately uniform for the longitudinal (ϕ) sweeps

360 points at 1° spacing for $-68^\circ < \theta < 68^\circ$

120 points at 3° spacing for $\pm 68^\circ \leq \theta < \pm 83^\circ$

40 points at 9° spacing for $\pm 83^\circ \leq \theta < \pm 88^\circ$

8 points at 45° spacing for $\pm 88^\circ \leq \theta \leq \pm 90^\circ$.

For the latitude (θ) sweeps, 1 point at each of the 180 longitudes is required, so linear interpolation in longitude is used to convert the reduced grid to the Cartesian grid. Overall, this procedure maintains full *linear* spatial resolution at all times.

- *Boundary Conditions.* The temporal boundary condition is an initial synoptic map $\mathcal{B}_r(x, y, 0)$ to start the computations. In practice, this is provided by an observed synoptic map from one of the observatories listed in Chapter 1. In the next section synthetic maps are constructed for the role of initial synoptic maps to test the implementation of the synoptic transport equation, whilst in the following chapter NSOKP synoptic maps are used in “real” data tests of the synoptic transport equation. In the spherical geometry, the pole is a singular point. The centres of the cells are situated at latitudes $89.5^\circ, 88.5^\circ, \dots, 0.5^\circ, -0.5^\circ, \dots, -89.5^\circ$ such that the cell boundaries are at integer values of latitude. Thus the cells surrounding the points closest to the pole are triangular, and there is no advection or diffusion of flux for the latitude (θ) sweeps at the poles. All transport at the poles takes place across the longitudinal boundaries. For the longitude (ϕ) sweeps, the right-hand boundary at $\phi = 360^\circ$ is critical since at most latitudes flux is swept across this boundary into the map by differential rotation. In previous studies the left- and right-hand boundary conditions were considered periodic, that is, the plots were wrapped around to feed the left-hand boundary conditions into the right-hand boundary conditions. But this is not a good choice of boundary conditions since the flux which leaves at the left-hand boundary during the simulation of a rotation does not re-enter at the right-hand boundary immediately but after a delay of one rotation. Fortunately, however, the initial map matches the synoptic map for the previous rotation at the right-hand boundary, thus if the two maps are pasted together and evolved simultaneously, the longitude 360° becomes internal and is evolved correctly. At the boundaries $\phi = 0^\circ$ and $\phi = 720^\circ$, a quadratic interpolation

formula is used to estimate the derivatives across these boundaries. The segment $360^\circ < \phi \leq 720^\circ$ is discarded after evolving for one rotation, so that accuracy at $\phi = 720^\circ$ is irrelevant, and numerical tests showed the accuracy of interpolation at $\phi = 0^\circ$, where there is predominantly an outflow, was sufficient over many rotations.

- *Time splitting in Multi-dimensions.* ETBFCT is a routine which is designed to integrate

$$\frac{\partial \rho}{\partial t} = -\frac{\partial}{\partial x}(v\rho)$$

from t_0 to t_1 . Define $\Delta t = t_1 - t_0$. If there are sources then

$$\frac{\partial \rho}{\partial t} = -\frac{\partial}{\partial x}(v\rho) + \rho \frac{\partial v}{\partial x},$$

that is,

$$\frac{\partial \rho}{\partial t} = -\frac{\partial}{\partial x}(v\rho) + S_x,$$

then the evaluation should be made at the half-time step $\Delta t/2$. This is performed by approximately solving

$$\frac{\partial \rho}{\partial t} = -\frac{\partial}{\partial x}(v\rho) + \tilde{S}_x$$

from t_0 to $t_0 + \frac{1}{2}\Delta t$ using \tilde{S}_x evaluated at t_0 . Then, the resulting $t_0 + \frac{1}{2}\Delta t$ value of ρ is used to evaluate $S_x(\Delta t/2)$. With this source term the equation

$$\frac{\partial \rho}{\partial t} = -\frac{\partial}{\partial x}(v\rho) + S_x$$

is subsequently solved again for the whole step. Now, in two-dimensions the integrations of

$$\begin{aligned} \frac{\partial \rho}{\partial t} &= -\frac{\partial}{\partial x}(v_x \rho) - \frac{\partial}{\partial y}(v_y \rho) + \rho \frac{\partial v_x}{\partial x} + \rho \frac{\partial v_y}{\partial y} \\ \frac{\partial \rho}{\partial t} &= -\frac{\partial}{\partial x}(v_x \rho) - \frac{\partial}{\partial y}(v_y \rho) + S_x + S_y \end{aligned}$$

are done successively; first integrate

$$\frac{\partial \rho}{\partial t} = \frac{\partial}{\partial x}(v\rho) + S_x$$

from t_0 to t_1 using half-time step evaluations of S_x , and then integrate

$$\frac{\partial \rho}{\partial t} = \frac{\partial}{\partial y}(v\rho) + S_y$$

from t_0 to t_1 using half-time step evaluations of S_y .

- *Flux Conserving Scheme.* The Fortran subroutine ETBFCT is a flux corrected transport scheme with estimates on antidiffusion corrections to prevent the build up of spurious maxima and minima. It was found that the antidiffusion flux created instabilities in the latitude (θ) sweeps at the polar boundaries, so the flux correction terms were discarded. The following tests demonstrate that there was no loss of accuracy.

5.2. A Synthetic Solar Model

This numerical scheme was tested on a simple synthetic model of the surface flux evolution over a cycle. The synthetic Sun surface was constructed using Snodgrass' [Snod83] differential rotation model and the DeVore *et.al.* [DeVo87] meridional flow model where the transport parameters were those determined by Cameron *et.al.* [Came98] and the diffusivity was taken to have the uniform value of $600 \text{ km}^2\text{s}^{-1}$. On the 180×360 latitude-longitude grid the distribution field was set to $B_r(x, y, t) = \cos(2x)$ with opposite polarity in the hemispheres. Babcock's model [Babc61] identified a number of relevant properties of the solar cycle. Sunspots occur in bipolar groups within zones parallel to the equator between $\pm(30 \pm 8)^\circ$. The bipolar groups have an orientation in which the "preceding" spots tend to be closer to the equator than the "following" spots. Accordingly these properties were incorporated in the synthetic model. At each time step, flux was injected at latitudes $\pm(15 \pm 17)^\circ$ with

an amplitude that varied sinusoidally with latitude. These quasi-active regions were given a tilt by adding an offset at 15.5° and subtracting an offset at 16.5° . The offset was of magnitude 0.1 and had the sign of the following polarity. Mathematically,

$$\begin{aligned} \pm (\cos(2x) \pm \text{offset}) \cos(\omega t) & \quad \text{at } \pm 16.5^\circ \\ \pm (\cos(2x) \mp \text{offset}) \cos(\omega t) & \quad \text{at } \pm 15.5^\circ \end{aligned}$$

where the sign of the offset is positive for the following polarity, and the sign of the whole term is positive in one hemisphere and negative in the opposite hemisphere. The injected flux was given a cyclic time dependence which had a cycle length of 3 years in order to reduce computational time.

The temporal diffusion term decrease in magnitude as the cycle increases in length. So the choice of a three year cycle provided a more stringent test for implementation than a solar-type cycle of 22 years. The preliminary numerical tests confirmed that the temporal diffusion terms were indeed negligible.

The synthetic Sun was evolved using the flux-transport equation until the flux distribution over the surface began to exhibit cyclic patterns. One such map, Figure 5.2, was selected as an initial surface flux distribution field and a set of instantaneous maps from this map were produced by applying the flux-transport equation with the transport parameters described before. Each rotational period was taken as 360 time steps so that synthetic ‘‘observed’’ synoptic maps, or reference synoptic maps, at 1° intervals of longitude could be constructed for successive rotations.

Solar cycle studies place much importance on the timing of polar reversals, thus the timing of polarity reversals in the following tests provides an indicator as to the accuracy of the method used for that test. In particular, the inclusion of the temporal diffusion terms did not affect the timing of the reversals, justifying their omission in general.

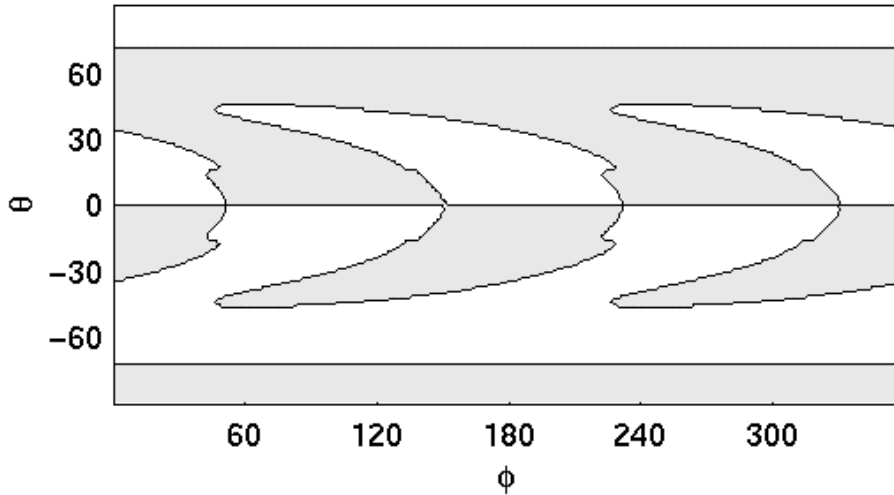


FIGURE 5.1. The initial surface flux distribution field which is a periodic map demonstrating properties of Babcock’s model. The solid lines correspond to zero-flux contours. The poles are unipolar regions of opposite polarity. The flux injected at $15^\circ - 17^\circ$ is spread and distorted by advection and diffusion.

5.3. Tests on the Synthetic Solar Model

A number of computational tests were used to compare the accuracy of the flux-transport equation scheme and the synoptic transport equation scheme. Both schemes were tested, firstly without flux injection, and then with flux injection. These two cases indicate that the synoptic transport equation is more accurate in simulating the evolution of the flux distribution when considering synoptic maps. Finally, the synoptic transport equation scheme was used in conjunction with random flux injection to determine if such random flux would affect the accuracy of the scheme.

5.3.1. No Flux Injection. A sequence of reference synoptic maps were produced using the flux-transport equation without sources. An initial double synoptic

map was chosen and evolved using the synoptic transport equation without the introduction of sources. Figure 5.2 shows a comparison of the simulated synoptic map and the “observed”, or reference, synoptic map at the polar reversal, which occurred after 6 rotations at around 60° longitude. The solid lines correspond to the zero-contours of the simulated synoptic map, while the dashed line corresponds to the zero-contours of the reference synoptic map. The zero-contours of the two maps are almost identical. This includes the polar contours, even though the polar fields are weak since the diffusion decays the initial field over time with no flux injection to replenish it. Figure 5.3 presents more detailed, equally spaced, contour maps for the maps in Figure 5.2. The upper panel is the reference map and the lower panel is the simulated synoptic map. As before, the two maps are almost identical except that between longitudes 0° and 90° the contour is discontinuous above latitudes of 60° in the reference map but is continuous in the simulated map. Also the polar line terminates, in terms of observation times, about 10° longitude later in the simulated synoptic map. This indicates that the simulated map has slightly less than the required diffusion, and the neglected temporal diffusion terms in the synoptic transport equation become significant for this level of accuracy.

5.3.2. Systematic Flux Injection. Now a sequence of reference synoptic maps was generated according to the model described in Section 5.2. As in the method introduced by Wilson and Giovannis [Wils94], new flux emergence was simulated by substituting reference synoptic flux for the simulated flux distribution between $\pm 30^\circ$ latitude at the end of each rotation. Panel (a) of Figure 5.4 is a comparison of the zero-level of the simulated (solid lines) and reference (dashed lines) synoptic maps. In this case, the synoptic transport equation was utilised to evolve the initial double synoptic map, without the continual flux injection, through to polar reversal. The simulations accurately match the polar zero-contour for the reference map. However,

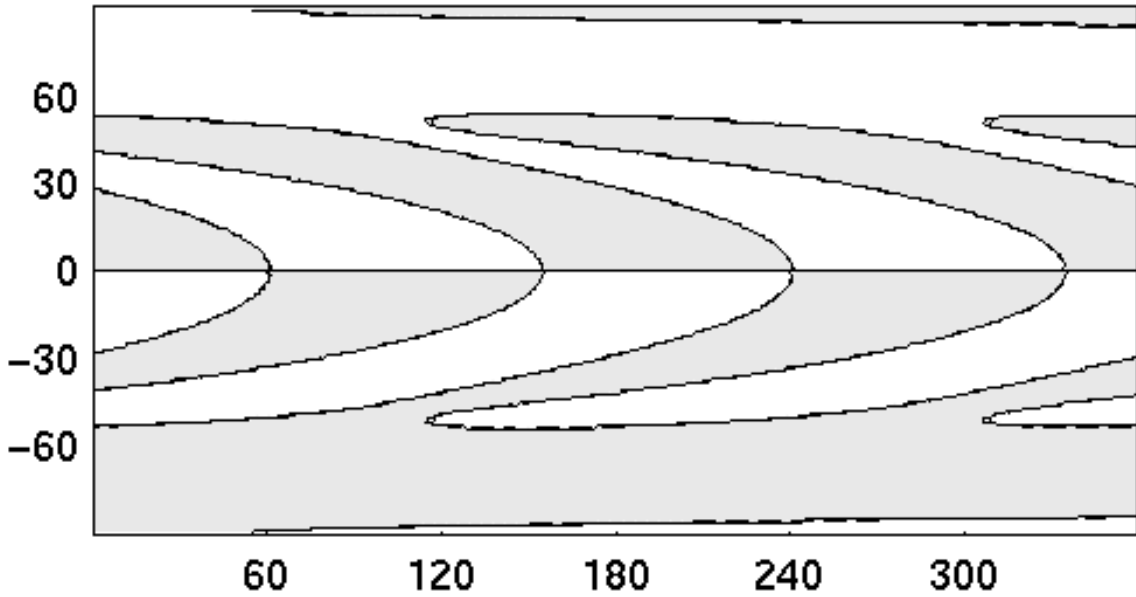


FIGURE 5.2. Synoptic maps produced from a synthetic solar model without sources of flux. The dashed line is the reference zero-flux contour, the solid line the zero-flux contour obtained by evolving a pair of initial synoptic map using the synoptic transport equation for 6 rotations.

in the equatorial region where flux was continually injected into the reference maps but not into the simulated maps, there is an expected discrepancy between the zero-contours for the two maps.

When the simulations include updated flux at the end of each rotation, the evolution of the reference synoptic maps is correctly described, as shown at the polar reversal in Panel (b). Figures 5.5 and 5.6 present more detailed comparison maps. The upper panels for both are the contour plots for reference map, and the lower panels are the contour plots for the simulated synoptic map. The contours in Figure 5.5 are taken at equal intervals between ± 1 , and to demonstrate the weak field structure the contours in Figure 5.6 are equally spaced between ± 0.12 . The simulation in both

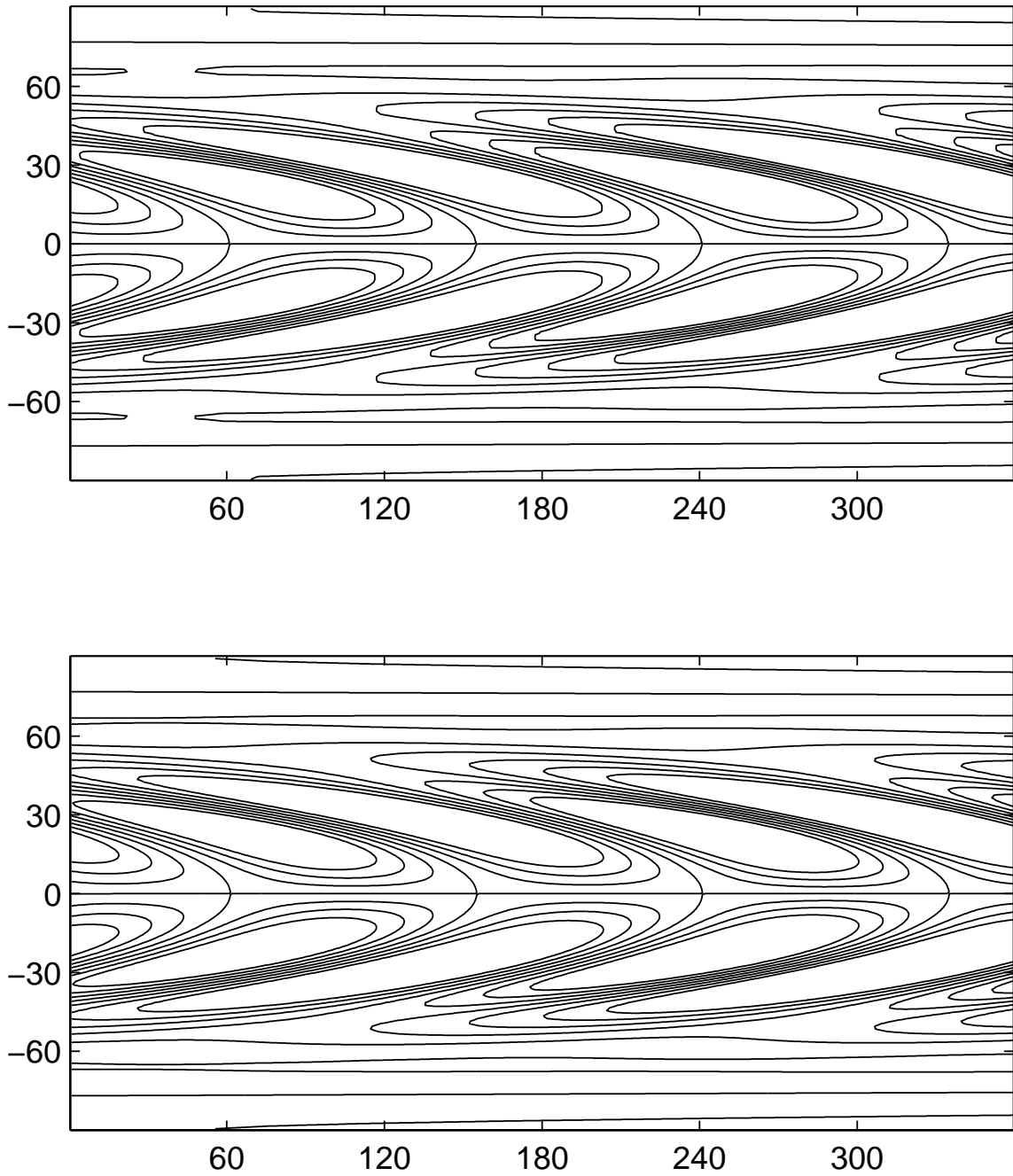


FIGURE 5.3. Synoptic maps produced from a synthetic solar model without sources of flux. The upper panel shows the reference map and the lower panel shows the approximate synoptic map from Figure 5.2. The contours are drawn at equal intervals.

comparisons accurately reproduces the reference map, except in the immediate region of flux injection.

Finally, the procedure employed by earlier authors was performed. The first map of the initial double synoptic map was evolved using the flux transport equation in conjunction with periodic boundary conditions and updated flux injection at the end of each rotation. Panel (c) of Figure 5.4 is a zero-contour comparison map of the flux transport simulated synoptic map with the reference map at the polar reversal. There are several significant discrepancies which occur at all latitudes, and are the result of the interplay of two effects.

Firstly, the enhanced drift and diffusion in the synoptic maps is neglected. As an illustrative example, consider a single flux feature near longitude 360° in the mid-latitudes of an initial synoptic map. Over a sequence of successive synoptic maps this feature will appear later for each rotation, that is, the longitude will decrease. During the rotation following the appearance of the feature close to longitude 0° , it will move across longitude 0° and become absent from the next synoptic map. Then one rotation later the feature will reappear near longitude 360° . Though two rotations will have passed, the feature will have moved in longitude and latitude distances appropriate to the time of one rotation, so it will have appeared that the latitude drift halted for one rotation. By evolving a double synoptic map as the initial map this is reproduced exactly. The flux which drifts out at 0° is replaced by flux drifting in at longitude 360° from the previous synoptic map at the appropriate lower latitude.

Applying the flux-transport equation in conjunction with periodic boundary conditions will result in the flux which drifts off at longitude 0° reappearing immediately at longitude 360° at the same latitude. This results in a steady drift of the pattern, with a lower speed than in the synoptic transport equation. This produces the same result in the end as the discontinuous drift with higher speeds, and so on average

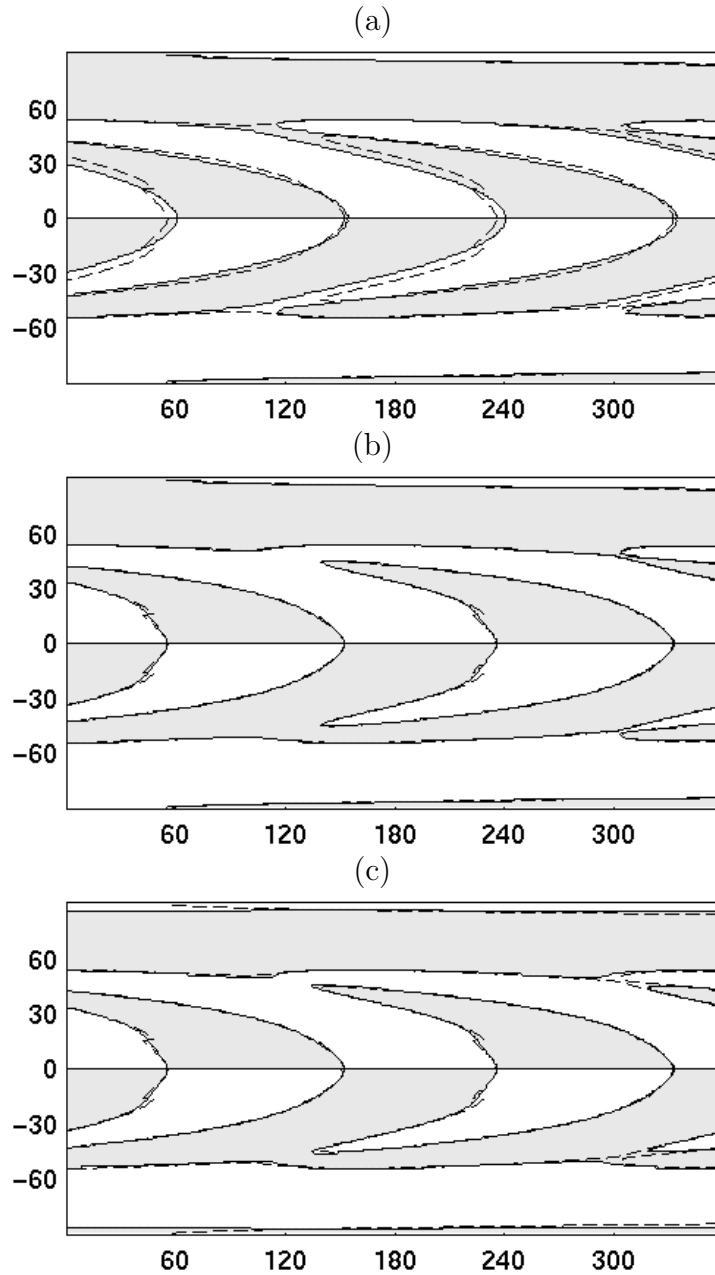


FIGURE 5.4. Synoptic maps produced from a synthetic solar model with systematic flux injection. The dashed line in each panel is the reference zero-flux contour, the solid line the zero-flux contour obtained by evolving initial synoptic maps. The upper panels shows the use the synoptic transport equation applied to two successive maps: panel (a) has no source updates, panel (b) updates the equatorial band every rotation. The lower panel (c) shows the use of the flux-transport equation with periodic boundary conditions and source updates every rotation.

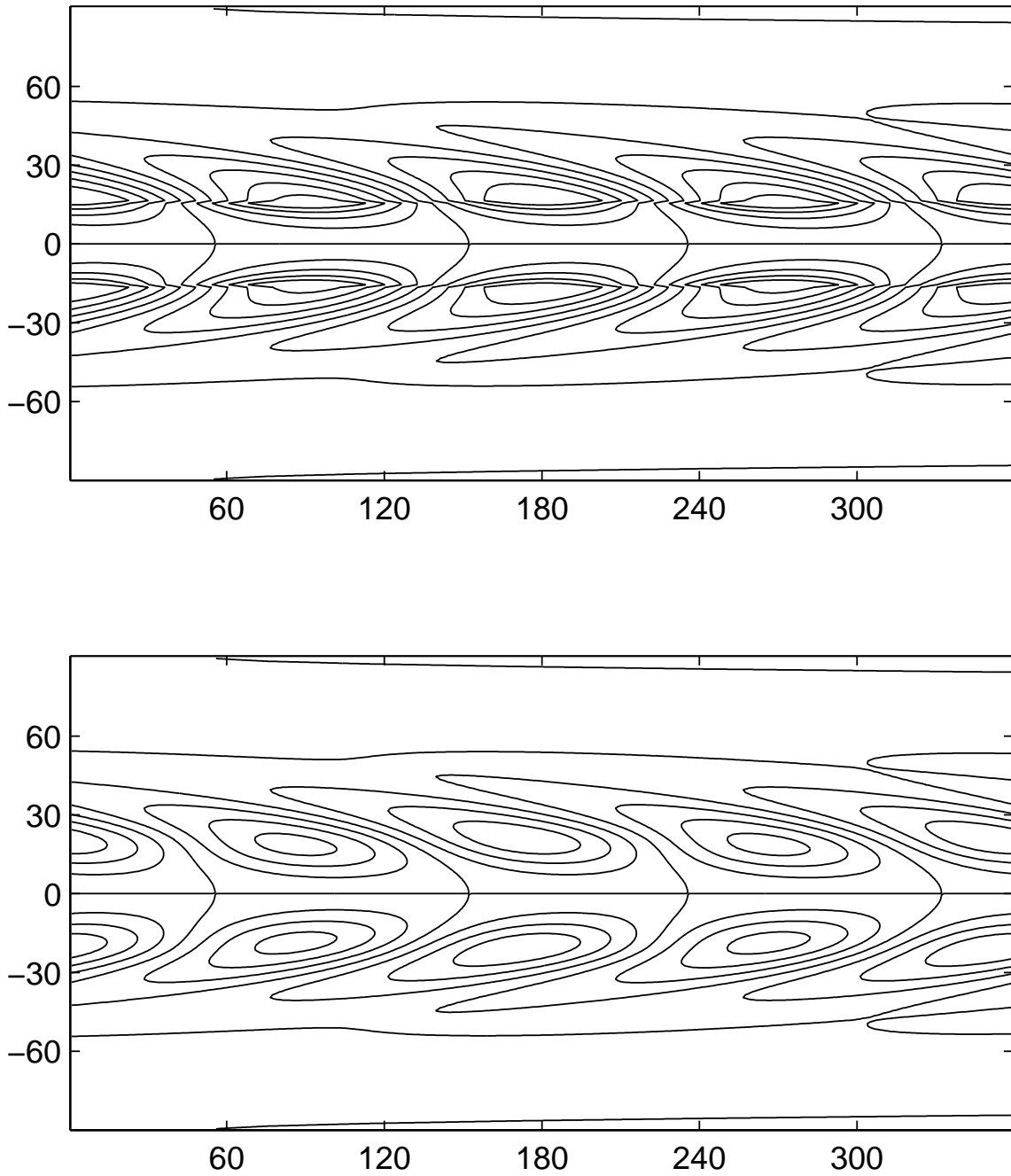


FIGURE 5.5. Synoptic maps produced from a synthetic solar model with systematic flux injection. The upper panel shows the reference map and the lower panel shows the approximate synoptic map from Figure 5.4(b). The contours are drawn at equal intervals between ± 1 .

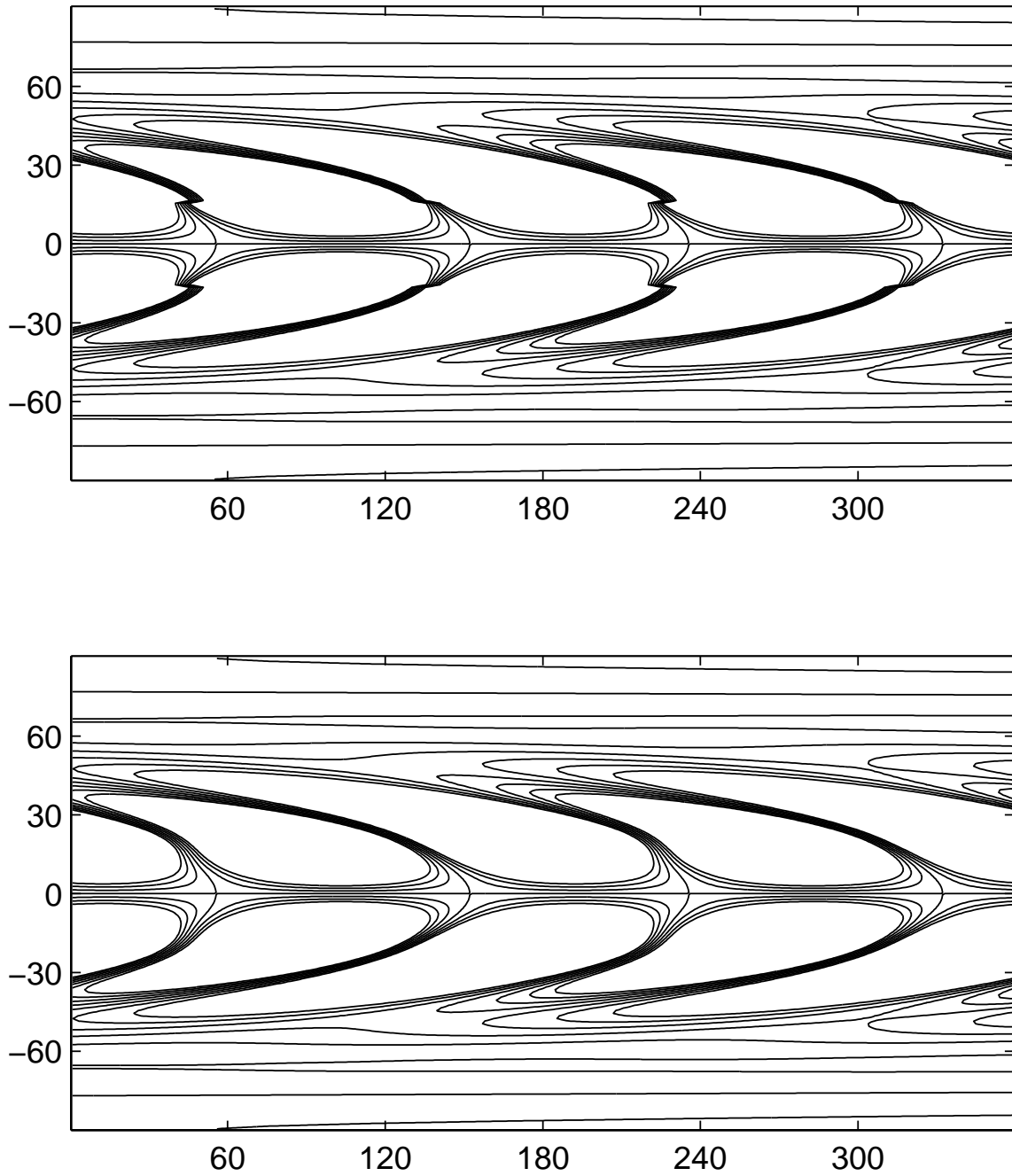


FIGURE 5.6. Synoptic maps produced from a synthetic solar model with systematic flux injection. The upper panel shows the reference map and the lower panel shows the approximate synoptic map from Figure 5.4(b). The contours are drawn at equal intervals between ± 0.12 , in order to show the structure of the weak fields.

the correct latitudinal drift is reproduced in both approaches. However, the periodic boundary conditions enforces a progressive symmetrisation of the flux distribution such that the zero contour is almost circularly symmetric in the estimate of the synoptic map. Furthermore, the drift and diffusion pattern is significantly underestimated at the lower latitudes where only small amounts of flux are “recirculated”.

5.3.3. Random Flux Injection. Finally, a sequence of reference synoptic maps were generated with random flux injection to simulate bipole eruptions. Every ten time steps during the evolution, a bipole was inserted in each hemisphere at a random longitude, and a random latitude between 0° and $+30^\circ$, and 0° and -30° .

The initial map of two successive synoptic maps was evolved using the synoptic transport equation. Figure 5.7 is the result for rotations four, five and six. As before, the simulated synoptic maps fail to reproduce the reference synoptic maps in the immediate region of bipole injection during a rotation. However, the flux distribution at the higher latitudes remains accurate, and in particular the polar reversal is accurately reproduced, similar to the results of the previous two tests.

5.4. Reconstructed Instantaneous Maps

The synoptic map can be defined in terms of the instantaneous map, as described by equation (4.14). The inversion of this map,

$$\bar{B}_r(\theta, \phi, t) = \mathcal{B}_r(\theta, \phi, t - (360^\circ - \phi)/\Omega),$$

provides a definition of the instantaneous map in terms of the synoptic map. Now an instantaneous map at the end of one rotation may be reconstructed by evolving the synoptic map, for that rotation, forward by one rotation. By taking the time step as $1/360$ of the rotation period, one longitude of the evolving synoptic map could be extracted per time step. The instantaneous flux along longitude 0° was extracted

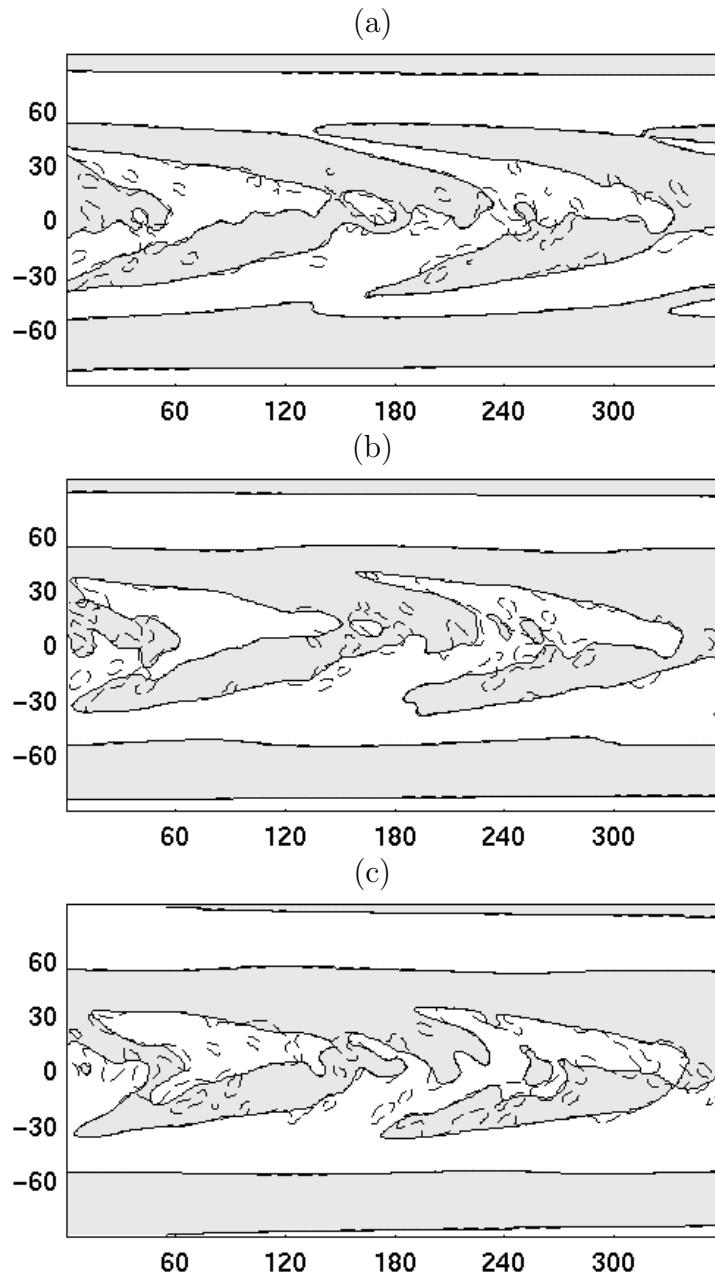


FIGURE 5.7. Synoptic maps produced from a synthetic solar model with random flux injection. The dashed line in each panel is the reference zero-flux contour, the solid line the zero-flux contour obtained by evolving the initial synoptic map. Panel (a) is after 4 rotations, panel (b) after 5 and panel (c) after 6 rotations.

from that longitude of the initial synoptic map. Then the instantaneous flux along longitude 1° is extracted from that longitude of the synoptic map evolved for one time step. This process is continued until the instantaneous map is completed at longitude 360° after 360 time steps. In principle, the instantaneous map should be exactly periodic, but if there are sources throughout the rotation then discrepancies will occur. Panel (a) of Figure 5.8 shows the reconstructed instantaneous map at the beginning of the rotation shown in Figure 5.4(b), and panel (b) of Figure 5.8 shows the reconstructed map at the end of that rotation. The polar reversal had occurred during that rotation. The zero-contour lines of the reconstructed instantaneous maps (solid line) reproduce the zero-contour lines of the observed instantaneous maps (dashed lines) very accurately at all latitudes, including the almost axisymmetric contours near the poles.

Figures 5.9 and 5.10 show the contour plots for the reference instantaneous map and the reconstructed instantaneous map illustrated in Figure 5.8(a). Figure 5.9 shows the strong fields and demonstrates that the amplitude of the reconstructed flux map is correct near longitude 0° but is too small in the equatorial regions at longitude 360° because these have been diffused for almost one rotation without replenishment. Figure 5.10 shows the weak fields. These are almost exactly reproduced in location and amplitude at all longitudes because they are not affected by the flux emerging in the course of the rotation.

This chapter has shown that the inconsistencies which appeared in the simple analytical model of Chapter 3 were due to two problems when the flux-transport equation was applied to synoptic maps. Firstly, when differential rotation is present there is an enhanced drift of features because of the fact that an element moving towards the pole takes increasingly longer to return to the meridian, which is not described by the flux-transport equation, and secondly the setting of the periodic boundaries

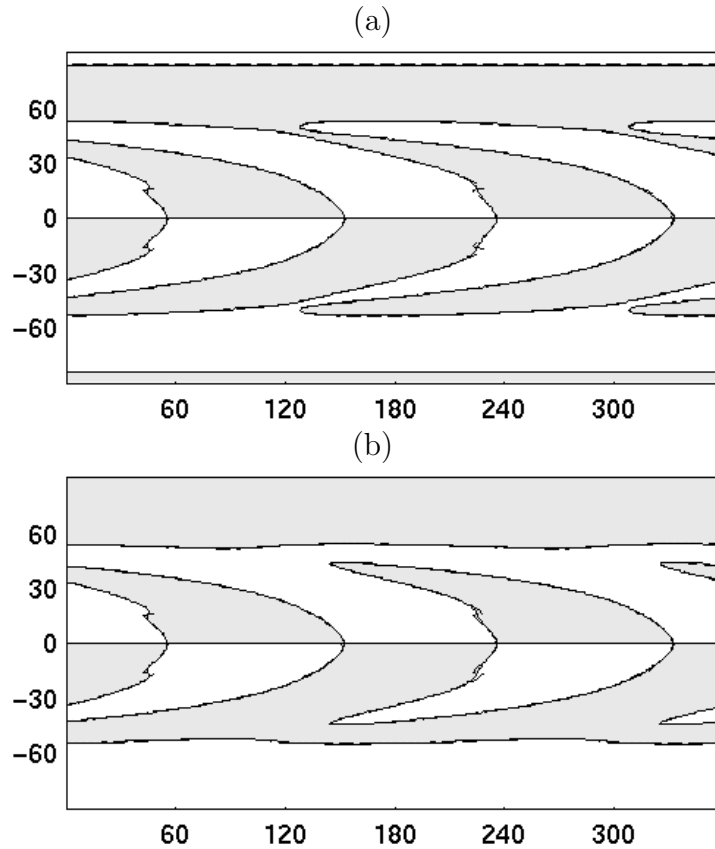


FIGURE 5.8. Reconstructed instantaneous maps. The dashed line in each panel is the true zero-flux contour, the solid line the zero-flux contour obtained from synoptic maps. The two panels show the instantaneous map at the beginning and end of the rotation shown in Figure 5.4(b).

conditions. In a synthetic solar model, it was shown that these errors are corrected by applying the synoptic transport equation to double synoptic maps, and that very accurate representations of “actual” synoptic maps can be produced. As a bonus, the synoptic transport equation provides a means of reconstructing instantaneous maps from synoptic maps. Although in a synthetic model the synoptic transport equation produces very accurate approximations, this implies nothing about the accuracy

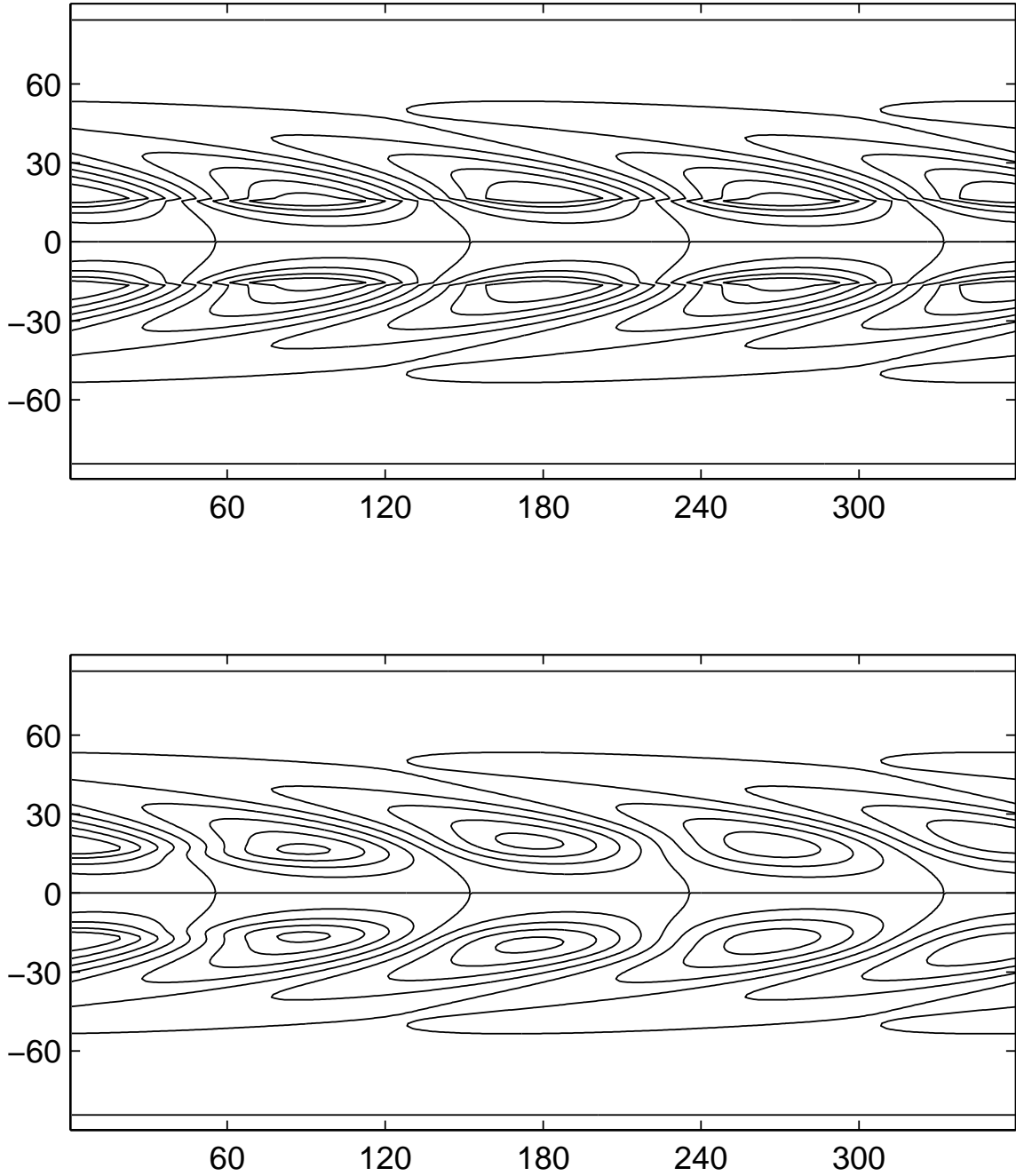


FIGURE 5.9. Instantaneous maps produced from a synthetic solar model with systematic flux injection. The upper panel shows the reference map and the lower panel shows the approximate reconstructed map from Figure 5.8 (a). The contours are drawn at equal intervals between ± 1 .

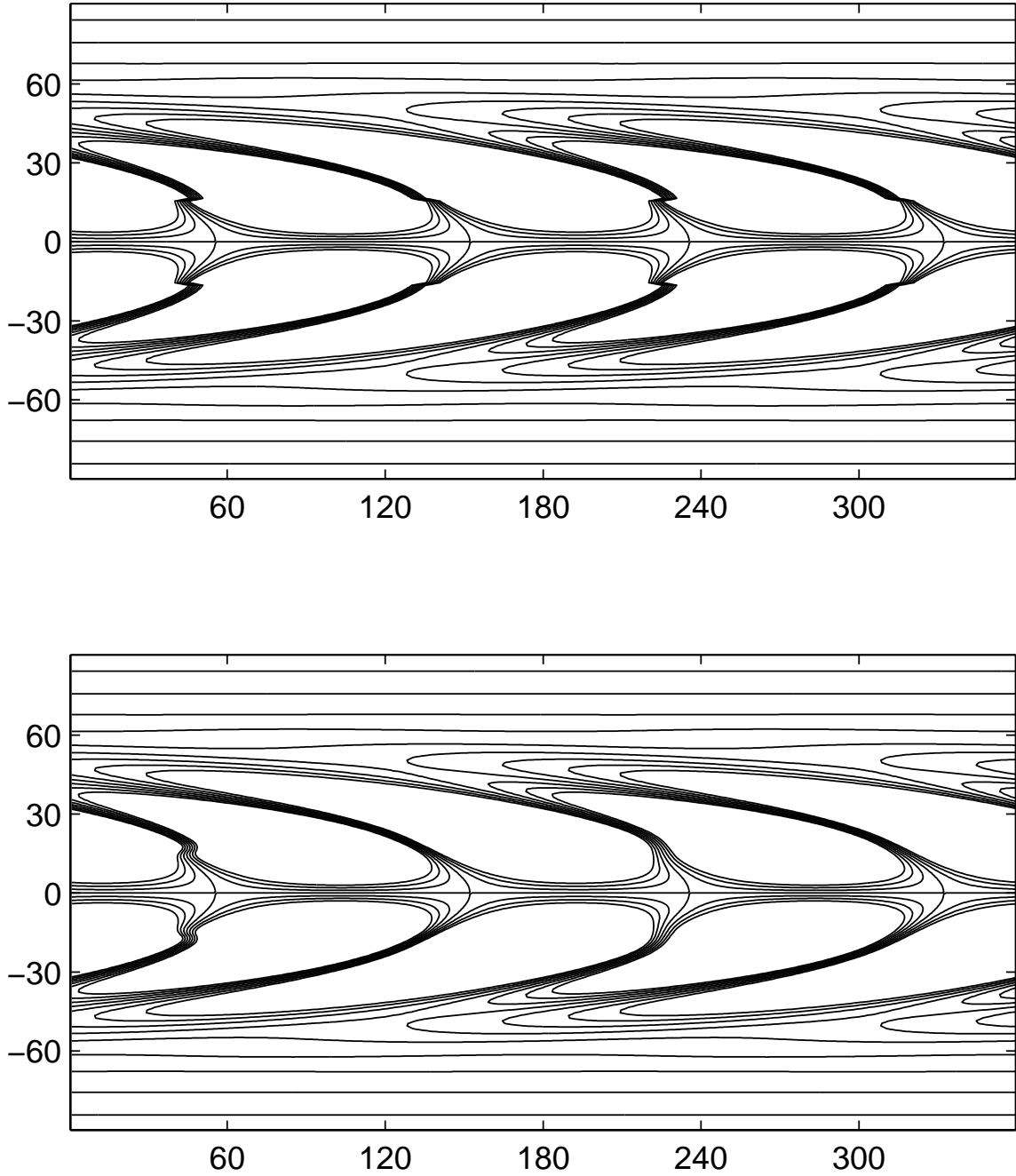


FIGURE 5.10. Instantaneous maps produced from a synthetic solar model with systematic flux injection. The upper panel shows the reference map and the lower panel shows the approximate reconstructed map from Figure 5.8 (a). The contours are drawn at equal intervals between ± 0.12 , in order to show the structure of the weak fields.

when considering “real data”. Chapter 5 examines the application of the synoptic transport equation scheme to synoptic maps from NSOKP.

CHAPTER 6

STE With Real Data

By utilising a synthetic solar model it was demonstrated in Chapter 5 that the synoptic transport equation scheme, not the flux transport equation, should be used to simulate the evolution of synoptic maps. Furthermore, the synoptic transport scheme produced extremely accurate results for the synthetic model. However, this conveys no information about the accuracy of simulations of “real” synoptic maps. Therefore, the final consideration for this thesis on the evolution of synoptic maps is to test the accuracy with which the synoptic transport scheme can simulate NSOKP observed synoptic maps, and reconstruct NSOKP instantaneous maps.

6.1. Simulating NSOKP Synoptic Maps

The polar axis of the latitude-longitude grid which is used for determining position on the solar surface is taken to be Sun’s rotation axis. The B -angle is defined as the angle of the tilt of this axis to the normal to the plane of the orbit of the Earth [Durr88]. The B -angle varies from 7.22° to -7.22° ; observations made when the B -angle is approximately these extreme values are said to be “favourable to the north” and “favourable to the south” respectively.

The most recent sequence of NSOKP synoptic maps from CR 1948 to CR 1990 was selected for this investigation. The synoptic maps for CR 1948 and CR 1949 were chosen to be the initial double map since the south was favourable during these rotations. This double map was evolved, according to the synoptic transport scheme described in Chapter 5, for a total of forty rotations. The only alteration made to the

scheme was to approximate the continual flux injection in active regions more realistically. Similar to the procedure utilised by Wilson and Giovannis *et.al.* [Wils94], at the end of each rotation the flux between latitudes $\pm 48^\circ$ (c.f. $\pm 30^\circ$ in Chapter 5) of the simulations was replaced by the flux distribution from the observed synoptic map for that rotation. Snodgrass's [Snod83] differential rotation model and the DeVore *et.al.* [DeVo87] meridional flow model were adopted, where the transport parameters were those determined by Cameron and Hopkins [Came98] and a uniform value of $600 \text{ km}^2\text{s}^{-1}$ was taken for diffusion.

A 1° resolution of the NSOKP synoptic maps was maintained for the application of the synoptic transport scheme. However, for the purpose of comparing observed synoptic maps with simulated synoptic maps, the observed maps were smoothed over a 15° radius circle with a cosine bell to ensure their resolution matched the resolution of the evolved synoptic maps. The solid lines in each comparison map correspond to the zero-contours of the simulated synoptic map, and the dashed lines correspond to the zero-contours of the NSOKP observed synoptic map. The white regions indicate positive polarity flux, and the shaded regions indicate negative polarity flux, for the simulated synoptic maps.

CR1951 is the second of the sequence of evolved synoptic maps, and the first illustrated in Figure 6.1. This observation was made when the solar equator was roughly in the ecliptic plane, and the flux from the equatorial region has not had enough time to diffuse very far. Therefore both north and south poles are reasonably represented in the observations. However, the high resolution data for these observations contain patches of opposite polarity near each pole. Traces of these are seen in the simulations of CR 1950, in the north, and CR 1952, in the south. These are not seen in the smoothed observations and disappear from the simulations when they are eliminated by diffusion.

Throughout the forty rotations the simulations represent the smoothed observed maps rather accurately. The drift of positive and negative flux from the active regions mimics the drift in the observations rather well, as postulated by Babcock [**Babc61**] and incorporated as a relevant factor in the NRL's flux transport equation [**DeVo84**]. The north and south poles become favourable three times each. The north pole becomes favourable at CR 1954, CR 1967 and CR 1981, and the migration of the north polar zero-contour is accurately produced at these times. Similarly, the south polar zero flux contour is produced accurately when the south pole is favourable, that is, at CR 1960, CR 1974 and CR 1987. When the B -angle is unfavourable several discrepancies occur in the polar observations. Firstly, in the north, at CR 1960 and CR 1961 the simulations and the observations are inconsistent, although they are consistent in CR 1959 and CR 1962. This suggests that the observational data is inconsistent from rotation to rotation.

There are also high-latitude positive flux patches which appear and vanish during CR 1973 - CR 1975. Discrepancies also occur in the south. For CR 1965 - CR 1968 structures do not repeat from rotation to rotation and the zero-contour varies erratically and does not match the south polar contour of the simulation. Large negative polarity areas appear consistently for CR 1980 - CR 1983 but are not present at CR 1979 or CR 1984.

Above 70° latitude the flux distribution is almost axisymmetric due to the fact that the diffusion and differential rotation are very effective at smoothing structures at these latitudes.

These inconsistencies would suggest that the polar observations may be unreliable. Without confirmatory evidence for large-scale changes in the flux distribution in the polar regions from rotation to rotation, it would follow that the synoptic transport scheme provides a means for constructing a more accurate synoptic map. Since the

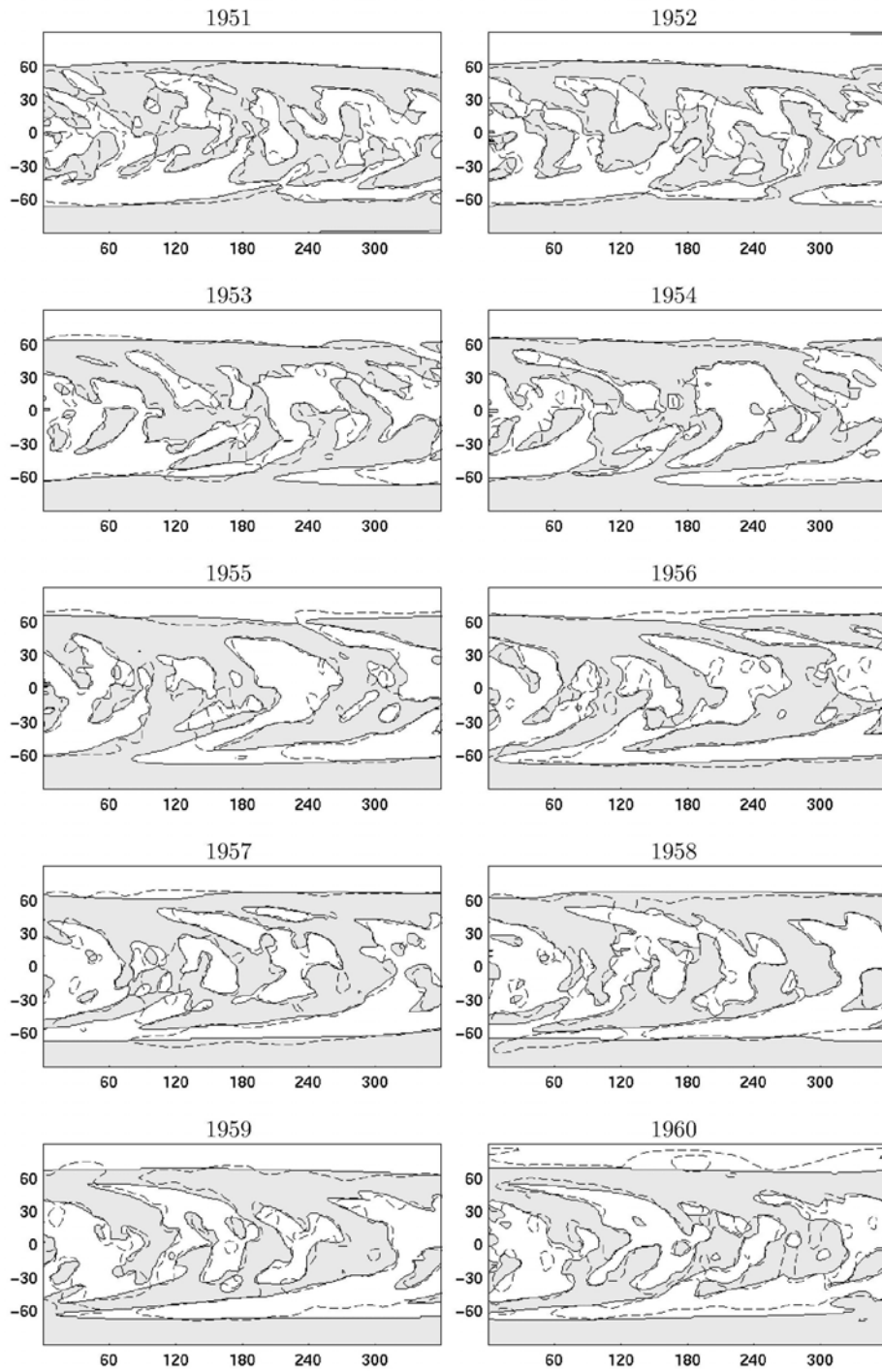


FIGURE 6.1. Comparison maps of NSOKP observed synoptic maps and synoptic transport scheme simulated synoptic maps for CR 1951 - CR 1960. See text for details of plots.

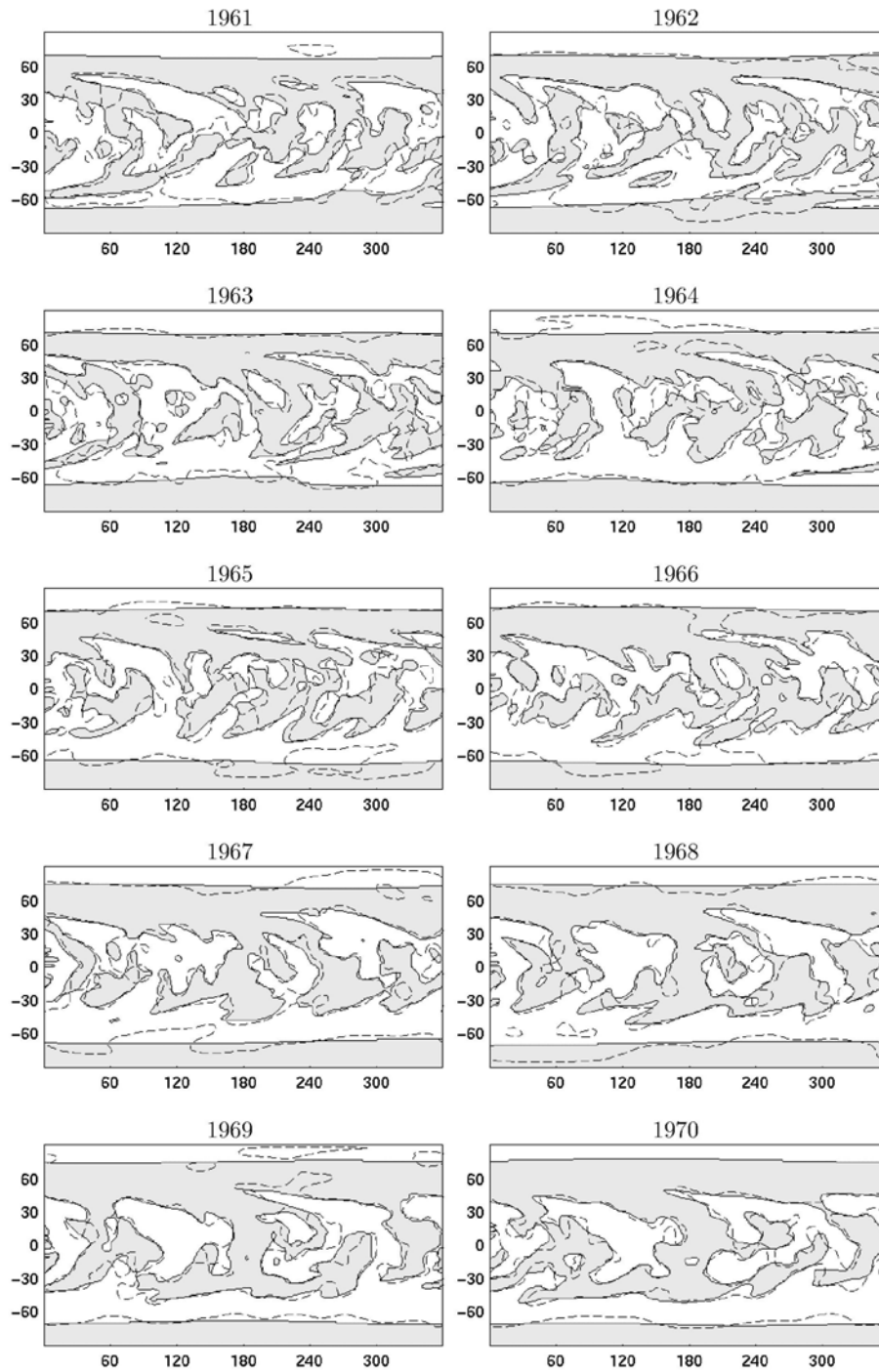


FIGURE 6.2. Comparison maps of NSOKP observed synoptic maps and synoptic transport scheme simulated synoptic maps for CR 1961 - CR 1970.

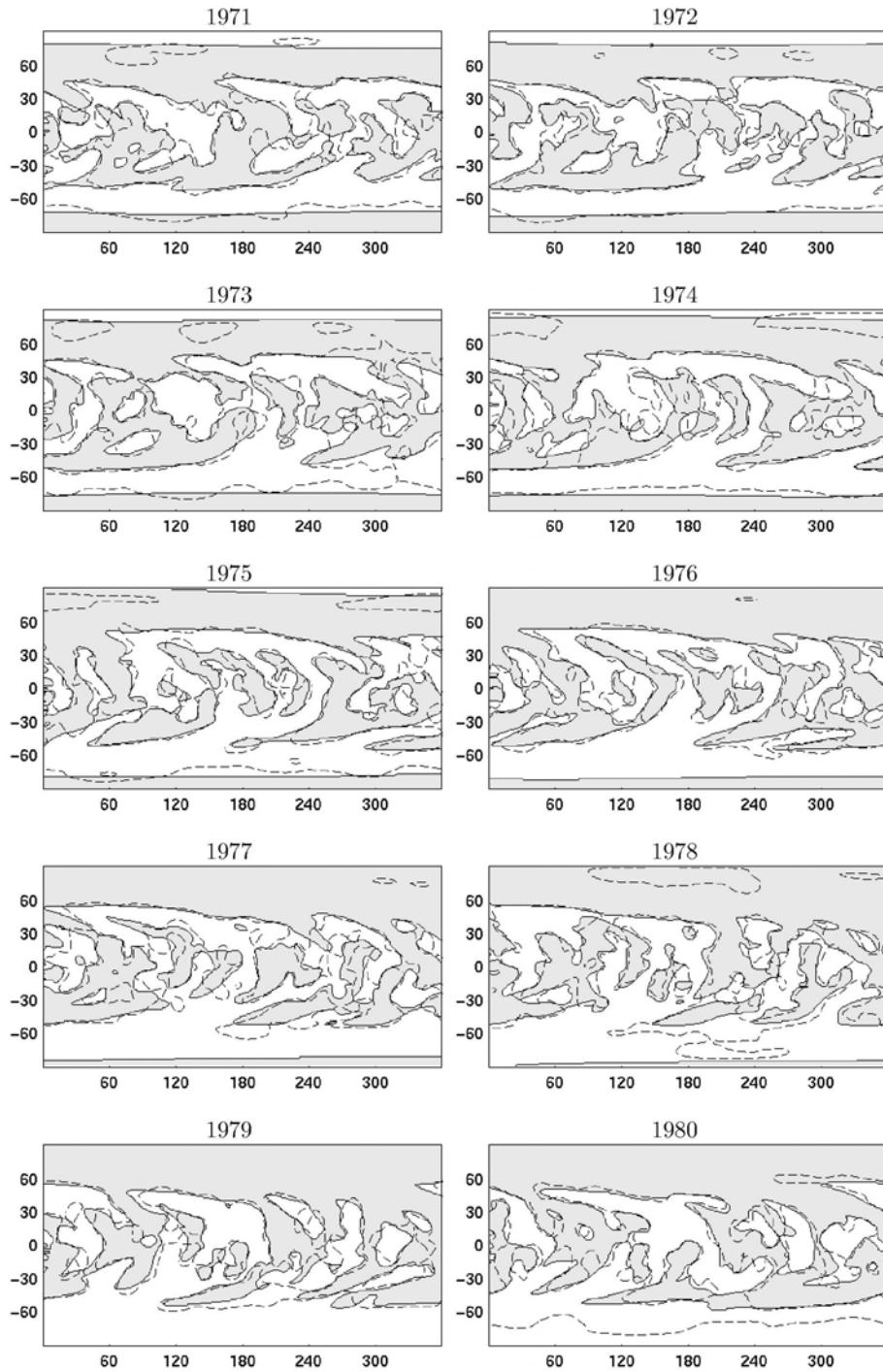


FIGURE 6.3. Comparison maps of NSOKP observed synoptic maps and synoptic transport scheme simulated synoptic maps for CR 1971 - CR 1980.

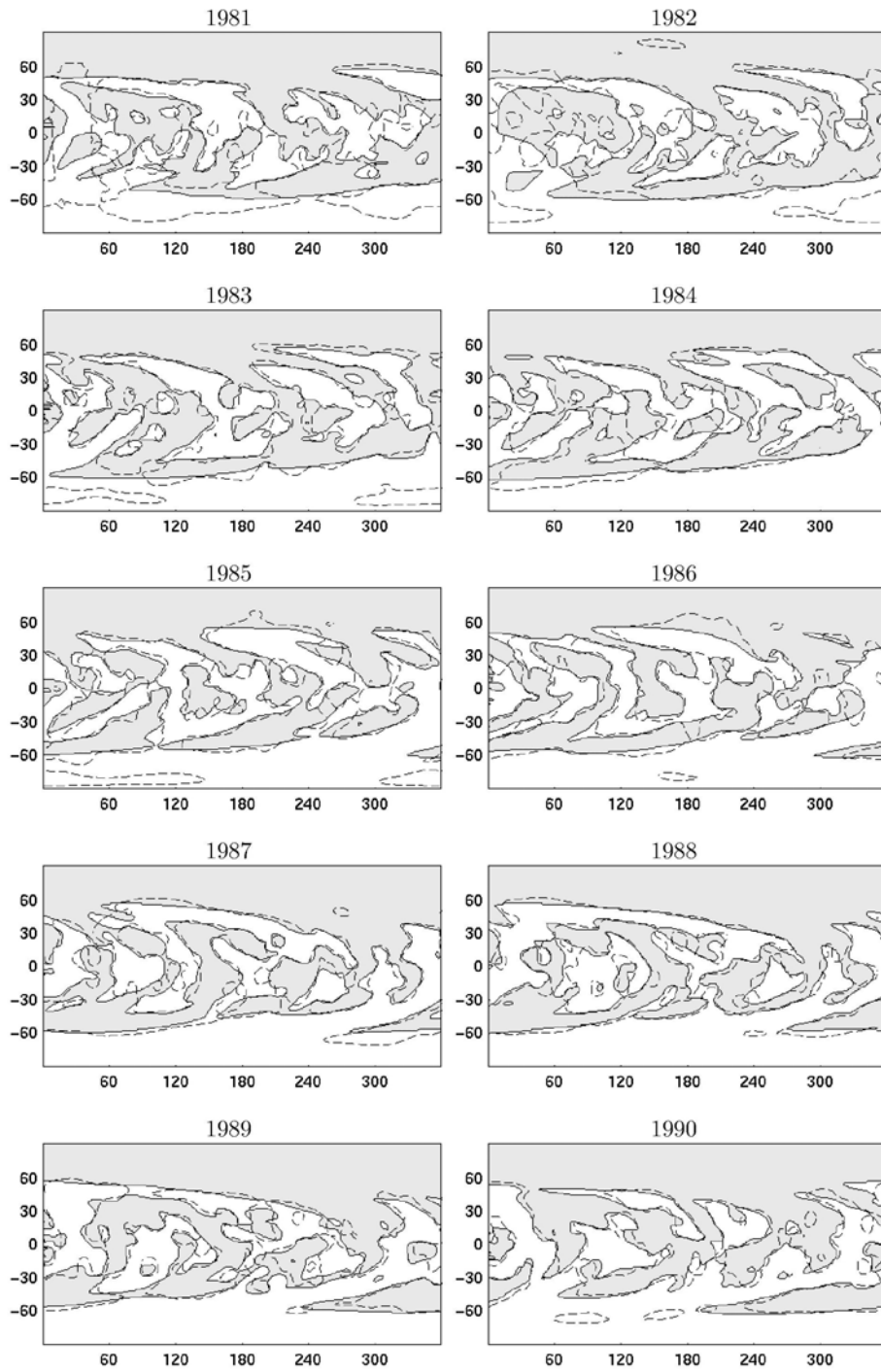


FIGURE 6.4. Comparison maps of NSOKP observed synoptic maps and synoptic transport scheme simulated synoptic maps for CR 1981 - CR 1990.

scheme produces accurate, reliable simulations and produces a smooth interpolation between reliable sets of observations, the polar reversals can be confidently determined from the simulations. The north pole is the first to go through a polar reversal, which occurs during CR 1975, and the south polar reversal follows during CR 1978.

However, it should be noted that a number of systematic deviations occur, for example CR 1953 - CR 1957 around latitude 50° south and longitude $120^\circ - 240^\circ$. Such deviations may be the result of high-latitude flux eruption as suggested by Wilson and collaborators.

6.2. Reconstruction of Instantaneous Maps

The procedure described in Section 5.4 for the synthetic model was used to reconstruct instantaneous maps from NSOKP synoptic maps. In Figure 6.2 the reconstructed instantaneous maps in the left sequence were generated when evolving synoptic maps over 360 time steps. The first of these reconstructed instantaneous maps is for the end of CR 1951. The 0° longitude for the reconstructed map is extracted from the 0° longitude of the initial synoptic map, longitude 1° is extracted from the 1° longitude of the synoptic map evolved for one rotation. This is continued until the synoptic map is evolved for 360 time steps at which point the 360° longitude is extracted for the reconstructed map 360° longitude. Similarly, the following three reconstructed instantaneous maps are generated for the next three rotations. To the right of each reconstructed instantaneous map is the corresponding partial instantaneous map generated from NSOKP magnetograms. Each instantaneous map was smoothed with a cosine bell of radius 15° . Points which are physically off the solar disc are represented by the darker grey region.

Depending upon longitude there is a variation in the resolution of the reconstructed map. At 0° longitude, no time steps have yet passed and there is no diffusion. After a small number of time steps there has been some diffusion applied to the flux injected between $\pm 48^\circ$ latitude but there has not been enough time to allow for the decay of this flux. Therefore there is a high resolution structure to the global features near 0° longitude. However, after 360 time steps without updating values between $\pm 48^\circ$ latitude, there has been enough time for diffusion to cause a greater differential smoothing than after a few time steps. Hence at longitudes near 360° there is a smooth structure about the global features.

Since the observed synoptic maps showed variations from rotation to rotation which were not present in the simulations, the daily maps would be expected to show even more variations. Structures near the centre of the instantaneous maps are rather similar in form and position for each case. But there are no obvious correspondences between the instantaneous and the reconstructed maps for latitudes $\gtrsim \pm 60^\circ$. In fact there are no polar contours present in the NSOKP instantaneous maps in the southern hemisphere, except for the slant from approximately -75° latitude to -60° latitude for the instantaneous map of 13 September 1999. By contrast in the reconstructed instantaneous maps there is a consistent polar line around -60° latitude. The instantaneous map corresponding to CR 1954 has a B -angle of 7.22° , such that the north pole is favoured, but discrepancies still occur between the observed and simulated maps in the northern hemisphere.

In conclusion, the synoptic transport scheme applied to a sequence of forty NSOKP synoptic maps produces accurate simulations throughout the forty rotations, which include simulating the polar reversals. Therefore, the numerical scheme presented here provides a reliable and robust procedure for simulating the evolution of synoptic

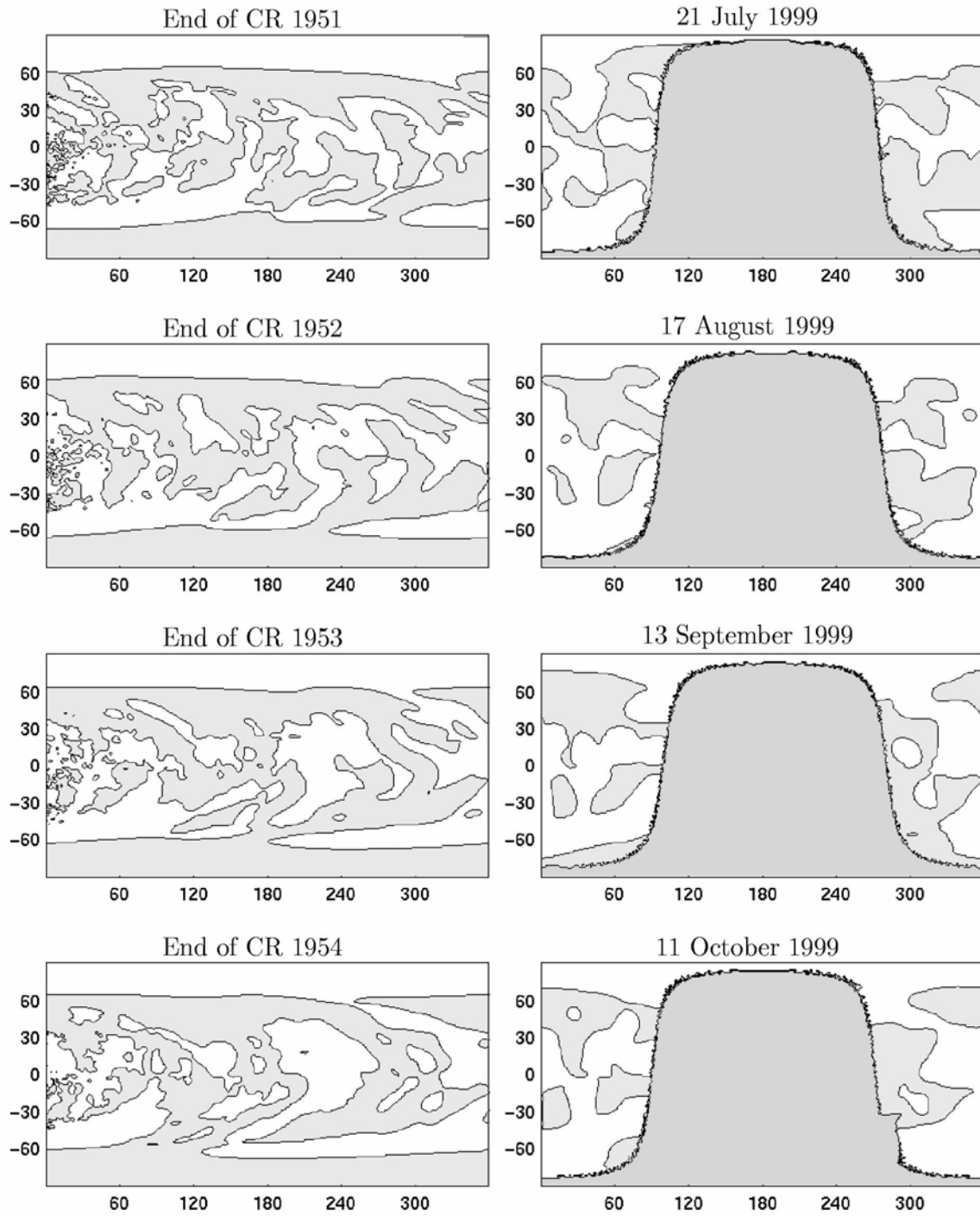


FIGURE 6.5. Comparing NSOKP observed instantaneous maps and synoptic transport scheme reconstructed instantaneous maps.

maps. The synoptic transport scheme in addition offers a reliable method for generating daily maps of the large-scale field, potentially of much greater accuracy than magnetograms. Finally, the synoptic transport scheme employs transport parameters derived by previous investigators independent of the use of the synoptic transport equation. These parameters were found to reproduce the longitudinal structures over the course of forty simulated rotations. As a consequence, the Snodgrass [Snod83] differential flow model, the DeVore *et al.* [DeVo87] meridional flow model, and the uniform value for diffusivity are further justified.

The implications of the results from Chapters 3, 4 and 5 upon previous studies of the evolution of the solar magnetic fields will be discussed in the following chapter.

CHAPTER 7

Conclusion

Babcock presented an empirical model of the solar cycle in 1961 in which he proposed the existence of a meridional flow. The discovery of a second convective circulating field, the supergranulation, prompted Leighton's heuristic model, in 1964, in which a diffusion equation was used to model the transport of flux. Supergranulation diffusion was the key form of the diffusive transport and was shown, at values of $800 - 12\,000 \text{ km}^2\text{s}^{-1}$, to be adequate to discount Babcock's suggested meridional circulation. However, by 1984 observational evidence of a meridional flow had increased to a level such that the NRL group incorporated meridional flow when deriving the flux transport equation. Since 1984, the flux-transport equation has been universally applied to magnetograms and synoptic maps in the study of solar surface magnetic fields.

However, it has been shown here in Chapter 3, by the use of a simple analytic model in a Cartesian system, that the flux transport equation fails to simulate an actual synoptic map and fails to derive true transport parameters when the flux-transport equation is applied to synoptic maps. Thus the assumption that the flux-transport equation may be applied to synoptic maps in the same way that it is applied to magnetograms is incorrect.

The synoptic transport equation was derived and compared to the flux transport equation in the implementation of the synthetic model in Chapter 5 in spherical coordinates system as described in Chapter 4. The effectiveness of the numerical scheme utilising the synoptic transport equation is due to two significant factors.

Firstly, boundary conditions were changed, from the periodic boundary conditions used in previous studies. By evolving two successive synoptic maps together where the 360° longitude of the latter synoptic map was equated with the 0° longitude of the earlier synoptic map, the need for artificial conditions at this boundary is eliminated. Flux moving into the latter map from the earlier map over one rotation drifts to the correct latitude. The boundary conditions at 0° and 720° were set by extrapolating internal data.

Secondly, the flux transport equation omits the new terms introduced into the induction by the transformation from the instantaneous flux B to the synoptic flux \mathcal{B} . The numerical scheme presented here in Chapter 4 uses a simplified version of the synoptic transport equation which neglects the two temporal diffusion terms, since they were shown to be rather small correction terms, but includes the third term. This third term alters the advection and diffusion according to latitude, and arises from the fact that points on the surface of the solar surface at the polar regions will take longer to return to the central meridian than those points in the equatorial region.

It is emphasised that, since the two temporal diffusion terms are neglected, the synoptic transport equation presented here is only an approximation of the solar case. Both order-of-magnitude considerations and numerical tests demonstrate that it is an accurate approximation in the case of the Sun.

The synoptic transport equation used on the synthetic solar model, described in Section 5.2, provided extremely accurate simulations in Section 5.3, and in comparison proved to be more accurate than simulations obtained by implementing the flux transport equation. This numerical scheme implementing the synoptic transport equation will reproduce the evolution of the solar magnetic fields given two assumptions. Firstly, the flux transport is properly described by advection and diffusion

alone. Secondly, the sources are restricted in latitudes such that they may be fully updated at each rotation. In Chapter 5, the simulations for the synthetic solar model had sources between $\pm 30^\circ$ latitude updated by observed synoptic maps between $\pm 30^\circ$ latitude at the end of each rotation. Similarly, simulations of the NSOKP synoptic maps, in Chapter 6, had sources between the more realistic latitudes of $\pm 48^\circ$ updated at the end of each rotation by observed NSOKP synoptic maps between $\pm 48^\circ$ latitude.

As indicated in Chapter 2, the flux-transport equation has been the key component of a large number of investigations of the solar surface magnetic flux in the last eighteen years during which it was liberally applied to magnetograms and synoptic maps. However, it has been demonstrated here that it is not correct to apply the flux transport equation to synoptic maps. This result is significant to a number of the studies mentioned in Chapter 2. The different approaches used in these studies are categorised here in order to simplify the process of identifying which are affected by this result.

Category I consists of those studies which involve the consistent use of magnetograms in solar surface structure and flow parameter studies. Any approach which involves the direct measurement of transport parameters by cross-correlating individual magnetograms, will produce true flow parameters and give the correct evolution of structures. The studies by Snodgrass [Snod83], [Snod91] and Snodgrass *et al.* [Snod96] are perfect examples of category I in which MWO magnetograms were cross-correlated to examine the differential rotation. Similarly, this procedure of determining the differential rotation was followed by Komm *et al.* [Kom93a] and [Kom93b] using NSOKP magnetograms. Deng *et al.* [Deng99] traced the motion of magnetic elements using longitudinal magnetograms from Huariou Solar Observatory Station in China and NSOKP full disc magnetograms to determine the rotation rate

between latitudes $55^\circ - 85^\circ$. Meridional flow studies utilising magnetograms were carried out by Snodgrass *et al.* [Snod96] and Komm *et al.* [Kom93c]. Other studies which are of category I are the investigations of the evolution of active region structures, such as that by DeVore *et al.* who compared magnetograms with the flux-transport equation, and most of the work in Sheeley *et al.* [Shee85], DeVore *et al.* [DeVo87] and Wang *et al.* [Wang90]. Schrijver [Schr01] performed simulations of photospheric magnetic activity by calculating a series of very detailed synthetic instantaneous maps using a model implementing the flux-transport equation, from which synoptic maps were constructed and compared with actual synoptic maps. This process used by Schrijver was generally similar to the procedure in which “true” synthetic synoptic maps were constructed in chapter 5.

Studies belonging to category II are those which utilised longitudinally averaged synoptic maps with the flux-transport equation and periodic boundary conditions. By integrating the synoptic transport equation over longitude (ϕ), boundary terms occur at $\phi = 0^\circ$ and $\phi = 360^\circ$ which do not cancel since the synoptic transport equation is not periodic. If the boundary conditions did cancel, then it would appear that transport of flux to the poles occurs at an enhanced rate, which is not the case. The correct boundary conditions will counterbalance this enhancement and produce an average drift equal to that appearing in the flux transport equation. Therefore the use of the flux-transport equation on symmetrised synoptic maps will mimic the polar motion of true synoptic maps, and yield the meridional flow parameters and the average evolution of the flux distribution. The work of DeVore *et al.* [DeVo84] is a Category II study. This was the first study of Leighton’s model which incorporated meridional flow as a component of the large-scale velocity field, and resulted in the flux transport equation. Also belonging to category II are the studies of the evolution of the Sun’s polar fields during sunspot cycle 21 by Wang *et al.* [Wang90], which

used longitudinal averages of the photospheric field, and the refinement of the DeVore *et al.* [DeVo87] model by Cameron *et al.* [Came98] in which the meridional flow was measured by calculating a least-squares fit to azimuthally averaged MWO synoptic maps.

Category III are the studies which applied the flux-transport equation in conjunction with periodic boundary conditions to synoptic maps in an attempt to obtain transport parameters and to study evolution of surface structures. It is these studies utilising synoptic maps that require the implementation of the synoptic transport equation. The factor $f(\theta)$, given by equation (4.18), is latitude (θ)-dependent, and will affect both the effective diffusion and advection. According to Snodgrass' [Snod83] differential rotation model, in the equatorial and sunspot zones $f(\theta) \simeq 1$ whereas at the poles $f(\theta) \simeq 1.40$, as can be seen in Figure 7.1.

Thus, since the flux-transport equation neglects this factor, the accuracy of the simulations based on evolving a synoptic map under the flux transport equation in conjunction with periodic boundary conditions will be affected according to which latitudes are considered. Investigations in the sunspot zones will suffer a small error but these errors will become progressively worse as the latitude approaches values of the polar regions.

The first study of the two-dimensional flux distribution utilising synoptic maps with the flux-transport equation was Sheeley *et al.* [Shee85]. The NSOKP synoptic map during CR 1646 was used as the initial surface flux distribution, then new sources were introduced according to the locations and times at which they appeared on the magnetograms. As noted in chapter 2, this work was extended by DeVore and Sheeley [DeVo87] and Wang *et al.* [Wan89b]. They suggested that discrepancies between their results and those found in DeVore *et al.* [DeVo85] were due to the fact that DeVore *et al.* [DeVo85] used NSOKP magnetograms for which the

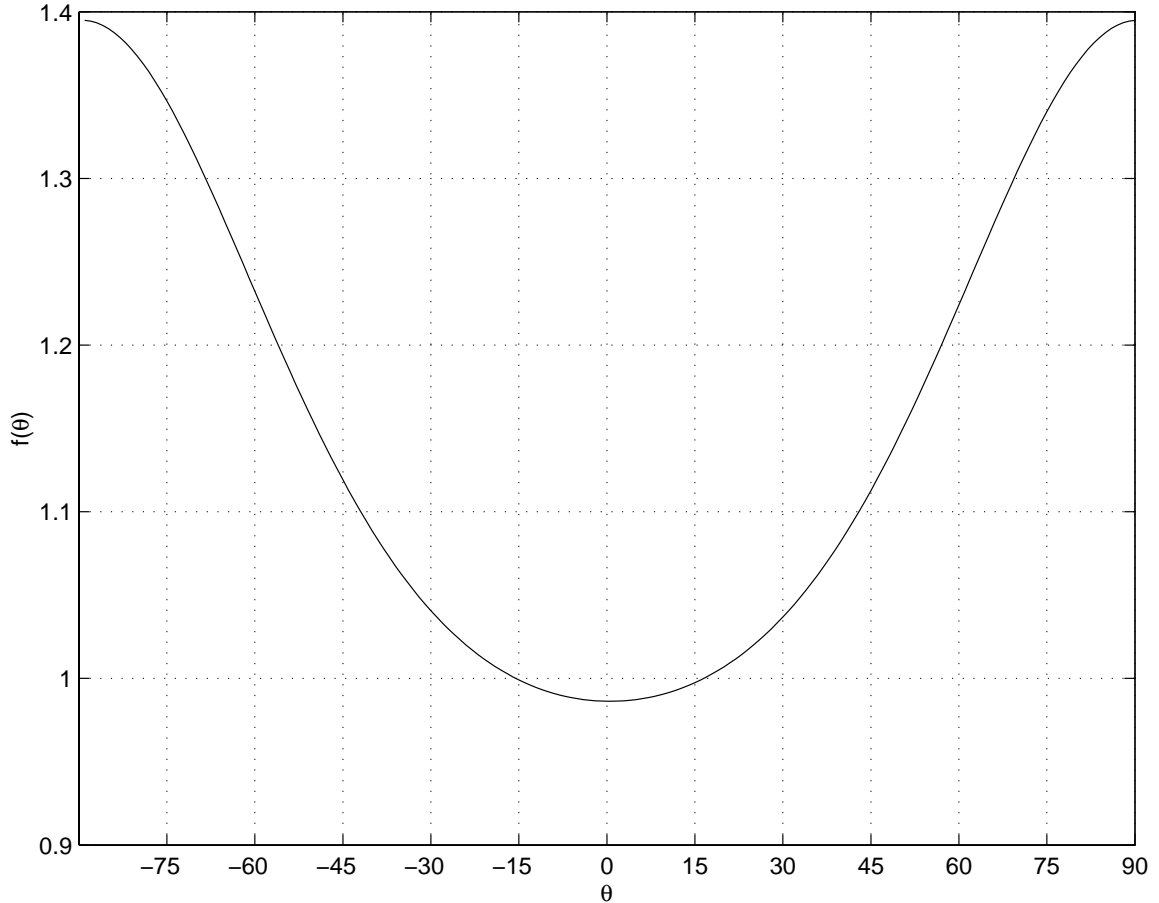


FIGURE 7.1. A plot of the latitude-dependence of the factor $f(\theta)$. In studies which rely on the flux-transport equation to simulate the evolution of synoptic maps, discrepancies between simulated and observed synoptic maps will increase up to a factor of 1.4 approaching the poles.

high-resolution data showed much smaller scale than can be reproduced with the use of the flux-transport equation. However it is more probable that these discrepancies are due to the application of the flux transport equation, instead of the synoptic transport equation, to synoptic maps by DeVore and Sheeley [DeVo87] and Wang *et al.* [Wan89b]. A longitudinal shift of 4° between NSOKP and simulations synoptic

maps was explained as a result of the use of a constant 27.275 day Carrington rotation instead of a period which might vary each year. However, as indicated in Section 2.4, Snodgrass found no evidence of rotation depending on time, so this explanation is inherently incorrect. A more significant discrepancy appeared at latitudes greater than 30° , as would be expected from the omission of the factor $f(\theta)$ which varies from ~ 1.05 for latitude 30° to 1.4 at the poles. This approach was continued by Wang *et al.* [**Wan89b**] and Wang and Sheeley [**Wang94**]. A number of new features were added to the implementation, such as non-uniform grids and the replacement of the diffusion constant by a discrete random walk process to model smaller spatial scales. These may have been introduced in an attempt to negate discrepancies between their results and those of previous studies which were based on magnetograms. But these may be unnecessary if the synoptic transport equation scheme described here is utilised, so their conclusions need to be re-examined.

This approach was then continued in an ensemble of investigations by Wilson and his collaborators. For each of the investigations by Wilson and McIntosh [**Wils91**], Wilson [**Wils92**], Murray and Wilson [**Murr92**], Wilson and Giovannis [**Wils94**] and Kress and Wilson [**Kres00**], the flux transport equation was solved numerically to simulate the evolution of the radial field. In each case an observed MWO synoptic map for a particular Carrington rotation was used for initial conditions. The investigation by Murray and Wilson was of the first studies in which emerging active regions were simulated by the cut and paste method in which the simulation data between latitudes $+50^\circ$ and -50° is replaced by the observed MWO values at each rotation. Wilson and McIntosh [**Wils91**] found several qualitative differences between the simulations and observed synoptic maps which could not be resolved by simply varying parameters of the flux-transport equation. Wilson [**Wils92**] examined one of these qualitative differences, and raised doubts about the validity of models reproducing active regions

using the flux-transport equation. Simulations of the polar fields and their reversal by Murray and Wilson [Murr92] could not accurately reproduce the observed polar field evolution and reversal, and this was also found to be the case by Wilson and Giovannis [Wils94] who concluded that “something is lacking in the flux transport model of the polar reversal”. Performing simulations of polar reversal, Kress and Wilson [Kres00] found that the inclusion of various patterns of emerging bipoles in the simulations makes it possible for the flux transport model to account for many features of the polar magnetic field. In contrast to these global simulations, Kress and Wilson [Kres99] investigated the life history of selected individual active regions implementing the same scheme as before except that NSOKP synoptic maps were used for initial conditions. Durrant *et al.* [Durr01] then examined the evolution of several high-latitude flux patterns, or “plumes”, and it was suggested that flux may emerge at latitudes above 35° on the solar surface.

These polar magnetic field studies, as indicated by Figure 7.1, the omitted factor $f(\theta)$ would range from 1.2 to 1.4, and thus the errors are more considerable. This effect of omitting this factor is shown by the results of simulations performed on the synthetic model in Chapter 5. In the case of Murray and Wilson [Murr92] and Kress and Wilson [Kres00], the flux-transport equation simulations utilising periodic boundary conditions showed polar reversals which lagged by a rotation behind the observed polar reversal. The implementation of the synoptic transport scheme provided more accurate polar reversal simulations. A re-assessment of the polar magnetic field studies is planned by Wilson and others.

Finally, Latushko [Latu93] and [Latu94] used MWO and NSOKP synoptic maps were used in a method which utilised cross correlation to study differential rotation. This investigation should be carefully analysed and re-assessed.

Investigations into the reasons for the inconsistencies identified here and in Chapter 6 are required. Firstly, it is suggested that, an examination of the procedures for transforming magnetograms to synoptic maps be conducted, possibly a joint investigation between the observatories who construct synoptic maps. Secondly it is suggested that investigations be conducted on the possibility of flux eruptions occurring in the polar regions as Peter Wilson and collaborators, for example Kress and Wilson [Kres99], have been investigating.

7.1. Concluding Remarks

The implementation of the synoptic transport scheme described Chapter 5 provides an accurate and robust means of studying the solar surface magnetic field. The key ingredients in the success of this computational scheme is the inclusion of the factor which arises under the transformation from the flux-transport equation to the synoptic transport equation which adjusts the advection and diffusion terms in a latitude-dependent manner. And secondly, the replacement of periodic boundary conditions used in previous studies by double maps, or two successive synoptic maps, which when evolved together ensure that accurate data drifts in from the right hand boundary of the synoptic map under investigation. This numerical scheme proved to extremely accurate over a seven rotation period for a synthetic solar model. During this period a polar reversal occurred and was simulated more accurately than the previously ubiquitously used flux-transport equation scheme. The application of the synoptic transport equation scheme to NSOKP synoptic maps, over a forty rotation period, demonstrated that the scheme was not only accurate in simulating actual observed synoptic maps but is also a very robust scheme. The improved accuracy of simulating the evolution of synoptic maps by the synoptic transport scheme over the flux transport scheme implies several previous studies require further investigation.

Finally, it has been suggested that the method for constructing observed synoptic maps and the presently accepted model of the solar surface magnetic fields both require consideration and possible improvement.

Bibliography

- [Babc53] Babcock, H.W. (1953) ‘The Solar Magnetograph’. *Ap. J.*, **118**, 387-396.
- [Babc61] Babcock, H.W. (1961) ‘The Topology of the Sun’s Magnetic Field and the 22 Year Cycle’. *Ap. J.*, **133**, 572-587.
- [Bori76] Boris, J.R. (1976) ‘Flux-corrected Transport Modules for Solving Generalised Continuity Equations’. NRL Memo Report #3237.
- [Came98] Cameron, R., and Hopkins, A. (1998) ‘A New Estimate of the Meridional Flow’. *Solar Physics*, **183**, 263-276.
- [Deng99] Deng, Y., Wang, J., and Harvey, J. (1999) ‘High-latitude Solar Rotation Traced by Magnetic Elements’. *Solar Physics*, **186**, 13-23.
- [DeVo84] DeVore, C.R., Sheeley Jr, N.R. and Boris, J.R. (1984) ‘The Concentration of the Large-Scale Solar Magnetic Fields by a Meridional Surface Flow’. *Solar Physics*, **92**, 1-?.
- [DeVo85] DeVore, C.R., Sheeley Jr, N.R., Boris, J.R., Young, T.R., and Harvey, K.L. (1985) ‘Simulations of Magnetic-Flux Transport in Solar Active Regions’. *Solar Physics*, **102**, 41-49.
- [DeVo87] DeVore, C.R. and Sheeley Jr, N.R. (1987) ‘Simulation of the Sun Magnetic Field During Sunspot Cycle 21’. *Solar Physics*, **108**, 47-59.
- [Durr88] Durrant, C.J. (1988) *The Atmosphere of the Sun*. Adam Hilgar, Bristol, England.
- [Durr01] Durrant, C.J., Kress, .J.M., and Wilson, P.R. (2001) ‘The Evolution of Trailing Plumes From Active Regions’, *Solar Physics*, **201**, 57-79.
- [Giov85] Giovanelli, R.G. (1985) ‘The Sunspot Cycle and Solar Magnetic Fields, I The Mechanism as Inferred Observations’. *Aust. J. Phys*, **38**, 1045-1066.
- [Grig92] Grigoryev, V.M., and Latushko, S. (1992) ‘E-W Motions of Large-Scale Magnetic Field Structures on the Sun’. *Solar Physics*, **146**, 239-245.
- [Howa83] Howard, R., Boyden, J.E., Brunning, D.H., Clark, M.K., Crist, H.K., and Labonte, B.J. (1983) ‘The Mount Wilson Magnetograph’. *Solar Physics*, **87**, 195-203.

- [Kom93a] Komm, R.W., Howard, R.F., and Harvey, J.W. (1993) 'Torosional Oscillation Patterns in Photospheric Magnetic Features'. *Solar Physics*, **143**, 19-31.
- [Kom93b] Komm, R.W., Howard, R.F., and Harvey, J.W. (1993) 'Rotation Rate of Small Magnetic Features from Two- and One-Dimensional Cross Correlation Analysis'. *Solar Physics*, **145**, 1-10.
- [Kom93c] Komm, R.W., Howard, R.F., and Harvey, J.W. (1993) 'Meridional Flow of Small Photospheric Magnetic Features'. *Solar Physics*, **147**, 207-223.
- [Kres99] Kress, J.M., and Wilson, P.R. (1999) 'The Evolution of Isolated Active Regions'. *Solar Physics*, **189**, 147-161.
- [Kres00] Kress, J.M., and Wilson, P.R. (2000) 'Simulations of the Polar Field Reversals of Cycle 22'. *Solar Physics*, **194**, 1-17.
- [Latu93] Latushko, S. (1993) 'The Relationship Between Meridional Drift and Rotation of the Large-Scale Solar Magnetic Field'. *Solar Physics*, **146**, 401-404.
- [Latu94] Latushko, S. (1994) 'Meridional Drift in the Large-Scale Magnetic Field Pattern'. *Solar Physics*, **149**, 231-241.
- [Leig64] Leighton, R.B. (1964) 'Transport of Magnetic Fields on the Sun'. *Ap. J.*, **140**, 1547-1562.
- [Murr92] Murray, N., and Wilson, P.R. (1992) 'The Reversal of the Solar Polar Magnetic Field; IV The Polar Fields near Sunspot Maximum'. *Solar Physics*, **142**, 221-232.
- [Shee85] Sheeley Jr, N.R., DeVore, C.R., and Boris, J.R. (1985) 'Simulation of the Solar Magnetic Field During Sunspot Cycle 21'. *Solar Physics*, **98**, 219-239.
- [Shee87] Sheeley Jr, N.R., Nash, A.G., and Wang, Y.-M. (1987) 'The Origin of Rigidly Rotating Magnetic Field Pattern on the Sun'. *Ap. J.*, **319**, 481-502.
- [Shee89] Sheeley Jr, N.R., Wang, Y.-M., and Harvey, J.W. (1989) 'The Effect of Newly Erupting Flux on the Field Coronal Holes'. *Solar Physics*, **119**, 323-340.
- [Schr00] Schrijver, C.J. (2000) *Solar and Stellar Magnetic Activity*. Cambridge University Press, Cambridge, UK.
- [Schr01] Schrijver, C.J. (2001) 'Simulations of the Photospheric Magnetic Activity and Outer Atmosphere Radiative Losses of Cool Stars Based on Characteristics of the Solar Magnetic Field'. *Ap. J.*, **547**, 475-490.

- [Snod83] Snodgrass, H.R. (1983) 'Magnetic Rotation of the Solar Photosphere'. *Ap. J.*, **270**, 288-299.
- [Snod91] Snodgrass, H.R. (1991) 'A Torosional Oscillation in the Rotation of the Solar Magnetic Field'. *Ap. J.*, **383**, L85-L87.
- [Snod96] Snodgrass, H.R., and Dailey, S.B. (1996) 'Meridional Rotation of Magnetic Features in the Solar Photosphere'. *Solar Physics*, **163**, 21-42.
- [Snod00] Snodgrass, H.B., Kress, .J.M., and Wilson, P.R. (2000) 'Observations of the Polar Magnetic Fields During the Polarity Reversal of Cycle 22'. *Solar Physics*, **191**, 1-19.
- [Wan89a] Wang, Y.-M., Nash, A.G., and Sheeley Jr. N.R. (1989) 'Evolution of the Sun's Polar Field During Sunspot Cycle 21: Poleward Surges and Long-term Behaviour'. *Ap. J.*, **347**, 529-539.
- [Wan89b] Wang, Y.-M., Nash, A.G., and Sheeley Jr, N.R. (1989) 'Magnetic Flux Transport on the Sun'. *Science*, **245**, 712-718.
- [Wang90] Wang, Y.-M., and Sheeley Jr, N.R. (1990) 'Magnetic Flux Transport and the Sunspot-Cycle Evolution of Coronal Holes and their Wind Streams'. *Ap. J.*, **365**, 372-386.
- [Wan91a] Wang, Y.-M., and Sheeley Jr, N.R. (1991) 'Magnetic Flux Transport and the Sun's Dipole Moment: New Twists to the Babcock-Leighton Model'. *Ap. J.*, **375**, 761-770.
- [Wan91b] Wang, Y.-M., Sheeley Jr, N.R., and Nash, A.G. (1991) 'A New Solar Cycle Model Including Meridional Circulation'. *Ap. J.*, **383**, 431-442.
- [Wang94] Wang, Y.-M., and Sheeley Jr, N.R. (1994) 'The Rotation of Photospheric Magnetic Fields: A Random Walk Model'. *Ap. J.*, **430**, 399-412.
- [Wils91] Wilson, P.R., and McIntosh, P.S. (1991) 'The Reversal of the Solar Polar Magnetic Field; II Simulations of the Large-Scale Field'. *Solar Physics*, **136**, 221-237.
- [Wils92] Wilson, P.R. (1992) 'The Reversal of the Solar Polar Magnetic Field; III The Large-Scale Fields and the First Major Active Regions of Cycle 22'. *Solar Physics*, **138**, 11-21.
- [Wils94] Wilson, P.R., and Giovannis, J. (1994) 'The Reversal of the Solar Polar Magnetic Field; V The Reversal of the Polar Fields in Cycle 22'. *Solar Physics*, **155**, 29-44.
- [Word00] Worden, J., and Harvey, J. (2000) 'An Evolving Synoptic Magnetic Flux Map and Implications for the Distribution of Photospheric Magnetic Flux'. *Solar Physics*, **195**, 247-268.

- [Web1] ftp://argo.tuc.noao.edu/SPMG_cdrom/README
- [Web2] ftp://howard.astro.ucla.edu/pub/obs/synoptic_charts/README.txt